2021

Directional Link Management using In-Band Full-Duplex Free Space Optical Transceivers for Aerial Nodes

A F M Saniul Haq
University of Central Florida

DIRECTIONAL LINK MANAGEMENT USING IN-BAND FULL-DUPLEX FREE-SPACE OPTICAL TRANSCEIVERS FOR AERIAL NODES

by

A F M SANIUL HAQ
M.Sc., University of Central Florida, 2021
M.Sc., Georgia Institute of Technology, 2015
B.Sc., Bangladesh University of Engineering and Technology, 2012

A dissertation submitted in partial fulfilment of the requirements
for the degree of Doctor of Philosophy
in the College of Optics and Photonics
at the University of Central Florida
Orlando, Florida

Summer Term
2021

Major Professor: Murat Yuksel

ABSTRACT

Free-space optical (FSO) communication has become very popular for wireless applications to complement and, in some cases, replace legacy radio-frequency for advantages like unlicensed band, spatial reuse, and enhanced security. Even though FSO can achieve very high bit-rate (tens of Gbps), range limitation due to high attenuation and weather dependency has always restricted its practical implementation to indoor application like data centers and outdoor application like Project Loon. Building-to-building communication, smart cars, and airborne drones are potential futuristic wireless communication sectors for mobile ad-hoc FSO networking. Increasing social media usage demands high-speed mobile connectivity for applications like video call and live video stream on the go. For these scenarios, implementation of in-band full-duplex FSO (IBFD-FSO) transceivers will potentially double the network capacity to improve performance and reliability of the communication link. In this work, we focus on implementing prototypes of FSO transceivers on mobile platform using both off-the-shelf and customized components. Current goal is to implement a prototype of IBFD-FSO transceiver using VCSEL as transmitter and PIN photodiode as receiver at 900 nm wavelength. We are considering atmospheric attenuation, FSO beam propagation model, geometry, and tiling of the components to optimize the link performance while keeping the package low-cost and mobile, ensuring connectivity to mass population. Eventually, our goal is to have communication between multiple airborne drones through IBFD-FSO transceivers by discovering each other and maintaining established link. Applications of this research is not only limited to the conceived idea of smart cities, but it can also have real impact on disaster management in times of wildfire or hurricane.

To my parents

who brought me in this world to see the light

ACKNOWLEDGMENTS

As I am getting closer to the end of my PhD journey, I came to realize this has been a collective endeavor, rather than my single effort. I have had tremendous amount of support, guidance, and encouragement from different walks of my life which pushed me to the point where I stand now.

I would like to thank Almighty Allah for His continuous blessings upon me, especially where my education is concerned. These five years of my PhD journey, though stressful sometimes, could not be easier if I had not have the mental strength provided by Him to cope with.

I would like to express my gratitude to my advisor Prof. Murat Yuksel for his endless support, encouragements, and appreciation since day one. I feel very lucky to have him as my advisor who has shown kindness and appreciation like no one else in my life. His constant push for excellence and amiable way of handling stressful situation have made this research possible. I would also like to thank my committee members Prof. Axel Schulzgen, Prof. Guifang Li, Prof. Kyle Renshaw, and Prof. Damla Turgut for their valuable feedback and suggestions.

Next I would like to acknowledge all my group members, without whom the journey would be impossible to finish. In the first year of my graduate life it was Dr. Mahmudur Rahman Khan, himself a graduate student then, who was my mentor. I learnt the basics of the free-space optics from him. I can't even keep count of how many times I have asked for his help not only about research, but also about various academic problems. Now when he is working as an Assistant Professor at York College, PA, he still manages time to help me with my research problems. I am eternally grateful for his support and this research would incomplete without his insights and efforts. I would also like to extend my gratitude to my other previous and current group members who were a constant support system through thick and thin: Dr. Mostafizur Rahman, Dr. Prasun Dey, Dr. Sifat Ibn Mushfique, Pooya Nabavi, Patrick De La Llana, Sayanta Seth, Shahzeb Mustafa,

Ammar Farooq, and Marc Jean.

I am very grateful to all the faculty members of CREOL, The College of Optics and Photonics, University of Central Florida. They made optics interesting through their innovative and exciting teaching methods. As a trained Electrical Engineer, the transition from engineering mindset to optics mindset was difficult. But it was possible due to the excellent courses and laboratory sessions designed and conducted by the CREOL faculty members. I would like to specially thank Dr. Ivan Divliansky for mentoring me during my TA assignments. I learned a lot of teaching techniques from him to make the classes interesting and engaging. I am also very grateful to the staff members and management team at CREOL, who has been extraordinary in helping out in every situation. I have never seen a better and efficient management team in my life in an academic setup.

Outside my research group at CREOL, UCF, I had the opportunity to interact with many researchers and mentors who inspired and encouraged me during my graduate studies. Dr. Yi-Che Lee and Dr. Tsung-Ting Kao are my first mentors in USA, while I came to Georgia Tech in 2014. They taught me a great deal in laboratory work and maintaining consistency in hardware research. I would also like to extend my gratitude to Dr. Khondker Zakir Ahmed, Dr. Faisal Ahmed, and Dr. Obaidul Hossen for their constant support and encouragement throughout my graduate studies.

My PhD journey was made possible through numerous courses and training throughout my academic career. I am grateful to all the faculties and instructors I had at the institutes I have attended: Bangladesh University of Engineering and Technology (BUET), Georgia Institute of Technology (GaTech), and University of Central Florida (UCF). I also had numerous study partners who were an important part of my learning process. I am thankful to each and every one of them for their enthusiasm and passion for education, which induced enthusiasm in me as well. I also fondly remember all my friends from all the institutes I have attended, who made the journey fun and memorable.

Finally, I would like to express my never-ending gratitude to my family. My parents, A K M Hafizul Haq and Shamsun Nahar, who have brought me in this world and never had a shred of doubt about my ability, even when I couldn't keep my faith. Their constant support, inspiration, and encouragement has fueled my journey. My Wife, Rudava Ullah, MD, has shown tremendous support and patience when I needed it most. She has always been a source of hope for me and propelled me towards the finish line. I am highly grateful to her. I am also thankful to my brother: A F M Ashikul Haq, MBBS, my sister-in-law: Mafruha Tumpa, MBBS, and niece: Afrah Shahrish Arshi, for always supporting my effort and inspiring me to succeed. I would also like to thank my in-laws: Md. Rahmat Ullah, MBBS, Fouzia Kasem, MBBS, Salmon Rahmat Ullah, and Fahim Rahmat Ullah, MBBS, for their support and believe in me.

TABLE OF CONTENTS

LIST OF FIGURES

LIST OF TABLES

CHAPTER 1: INTRODUCTION

Free-space-optical communications (FSOC) is envisioned to play a significant role in future generation wireless ad-hoc networks (Figure 1.1). FSO network can be a useful for multi-node short distance communication network, which requires high bandwidth and mobility. Tactical ad-hoc networks with requirement of high bandwidth and reduced probability of jamming and interception can greatly benefit by implementing nodes with FSO transceivers. Beyond these advantages, the network capacity can be significantly increased by utilizing the FSO transceivers for in-band full-duplex communications. In recent years, the application of FSO transceivers has attracted strong interest from both the wireless research community and industry [2, 3, 4]. FSOC uses the unlicensed optical spectrum and relies mostly on the basic optoelectronic technology used in fiber optic communications. It provides very high point-to-point data transfer rate (up to 10 Gbps) [5] and much higher bandwidth compared to traditional RF networks. Moreover, FSO transceivers are highly directional, and thus, provides better spatial reuse and larger network capacity. This directionality also reduces the inference caused from unwanted directions and enhances signal security by lowering the probability of interception and detection by sniffers.

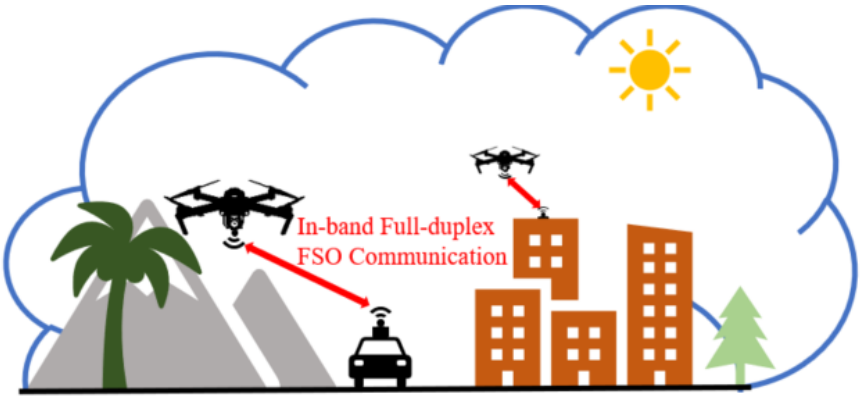

Figure 1.1: In-band full-duplex FSO communication between mobile nodes

Currently, in almost all the communication networks the antennas/transceivers operate in half-duplex mode, where a node can either transmit or receive but cannot do both over the same communication channel at the same time. Although, this results in inefficient use of resources, it helps to avoid self-interference that occurs when the mode of operation is full-duplex. In-band full-duplex (IBFD) communication uses simultaneous signal transmission and reception in the same frequency band. Despite the disadvantages caused by self-interference, full-duplex operation can aid in successfully dealing with huge spectrum demands. Although full-duplex communication provides increased wireless channel capacity, it is prone to more interference compared to half-duplex communication. In [6], it has been shown that, even in the presence of interference, full-duplex communication can provide at least 20% gain over half-duplex communication. A new MAC protocol for full-duplex radio communication is proposed in [7] that helps achieve 88% throughput gain. Also, the effect of interference reduces significantly with increase in directionality of the transmitter and the receiver of a node [8]. Recently, several other works have focused on designing directional RF transceivers showing the feasibility of having full-duplex communication [9, 10].

For RF transceivers, full duplex (FD) communication can be achieved through active or passive self-interference suppression. In *active* interference suppression, a node cancels out its own transmitted signal received by its receiver by injecting a cancelation waveform in the direction of its own receiver antenna. In *passive* suppression, transmitter and receiver antennas are separated by an electromagnetic observer which enforces the signal strength at the receiver coming from its own transmitter to be below receiver cutoff [10]. For FSO transceivers, full duplex communication can be achieved by using transmitters and receivers of separate wavelengths [11, 12, 13]. The idea of isolating the transmitter and receiver of a node using non-reflective and non-transparent material for achieving in-band full-duplex functionality has been proposed in [14, 15, 16]. But, to the best of our knowledge, there has not been any prior work demonstrating a functional IBFD transceiver

particularly within the context of mobile FSO networks.

Mobile FSO networks can be a useful solution for multi-node, high speed, short distance communication. Tactical ad hoc networks with requirement of high bandwidth and reduced probability of jamming and interception can greatly benefit from implementing nodes with FSO transceivers [3]. Beyond these advantages, the network capacity can be significantly increased by utilizing the FSO transceivers in an IBFD manner. Some of the drawbacks of IBFD FSOC can be addressed implementing multi-element transceiver nodes with capability of spatial reuse, beam steering, cognitive techniques for adaptive optimizations, and tolerance to mobility, vibration, sway, or tilt during communication. The single most *key limitation of the mobile FSOC is to maintain the link under perturbation*. Loss of LOS might result in loss of communication, and hence the alignment of the transmitter and receiver might need to be compensated for vibration, sway, or tilt. Intelligent design of a multi-element transceiver plane layout may minimize these loss components and maximize signal-to-interference and noise ratio (SINR) for mobile FSOC links.

On the other hand, FSO-enabled UAVs are envisioned to play a significant role in future generation mobile wireless ad hoc networks. Swarms of UAVs connected to each other via FSOC links can help to relay data from pico-cells to the core network. UAVs are also used for both civil and military missions, such as monitoring of an area hit by a natural disaster, broadcasting data at some critical sports event or even observing behind the enemy lines. Recently, Alphabet Inc. deployed stratospheric solar-powered balloons to provide Internet service to remote areas of Puerto Rico where cellphone towers were damaged by Hurricane Maria. All these different applications of UAVs produce large amounts of data that is required to be delivered to a ground station or other UAVs [17]. Using FSO transceivers, these large volumes of data can be transferred at extremely high speeds. Directional FSO antennas also provide secure communication compared to traditional omni-directional link. Directional antennas reduce possibility of receiving data from unwanted direction as well as makes it difficult to intercept and detection by sniffers. Even with so

many advantages, communication using directional transceivers are limited by line-of-sight (LOS) alignment. Even if the transceivers are within communication range, they can not establish a link if they are not facing each other. For this very reason, directional neighbor discovery is the first step to establish a directional communication link.

1.1 History of Optical Communication

Optical communication is an ancient medium of communication. Ancient Romans and Greeks used fire as a signalling tool around 800 BC. Even though the information transmitted were pretty low, it was a very effective way of signalling danger and crucial for survival. By the time 150 BC, American Indians were also adopting smoke signal for the same purposes. Light pulses were also used to communicate between ships at the ocean for distress call or emergencies. The first use of light as optical communication as we know today was the photophone experiment by Alexander Graham Bell in 1880 [18]. In this experiment, solar radiation was used to modulate information and transmitted over a distance of 200 m. However, the robustness of the system was too low to sustain reliable connection. FSO communication became more accessible and reliable with the invention of laser in the 1960s. Many prominent research groups, including MIT Lincoln Laboratories, North American Aviation, and Nippon Electric Company (NEC) led the way to demonstrate long-range laser-based communication channels. Around 1970, NEC demonstrated commercial laser-based FSO communication link between the cities Yokohama and Tamagawa using a full duplex 0.6328 μm He-Ne laser.

FSO and OWC has been of great interest to researchers and mostly funded for military covert applications. This technology has also been of interest for deep space communication. NASA explored OWC for Mars Laser Communication Demonstration (MLCD) and paved many other suitable applications for optical communication channels. The first open standard for infrared

(IR) data communication was established by The Infrared Data Association (IrDA) in 1993 [19]. It took more 15 years to establish global standards for home networking using IR and visible light communication (VLC). In 2009, standard for VLC (IEEE 802.15.7) was introduced. Due to many challenges and lack of technological maturity, integration into the existing communication networks has been slow for FSO systems. However, in recent years, FSO technology has seen a significant increase in technological maturity and culminated into increased commercialization and integration into today's communication infrastructures [20].

1.2 Advantages of FSO Communication

With increasing wireless data demand and exponential increase of mobile devices, OWC offers the necessary bandwidth and speed that requires to fulfill the demand. OWC avails a wide range of diverse applications that span from on-chip optical interconnects (mm range) for integrated circuits [21] to intersatellite communication links (km range) [22]. In 2017, hurricane Maria devastated Puerto Rico and left millions of people with no power and emergency connections. Google's Project Loon provided emergency connectivity to the people of Puerto Rico including LTE support to emergency responders and general public. The balloons used for Project Loon had multi-hop optical communication between the balloons. FSO systems offer many advantages for such applications:

- *Spatial Reuse:* Due to the smaller divergence angle, multiple channels can be accommodated. Also, higher capacity per unit volume sharing same frequency gives rise to higher bandwidth. Further, well-defined beam path ensures reduced interference.
- *Data Transfer Rate:* FSO provides the potential for higher data transfer rate with unregulated and unlicensed bandwidth. Due to no utilization tariffs, FSO makes it possible to meet the

high data demand with very little additional cost.

- *Security:* FSO offers highly secure connectivity. The optical beams are narrow and invisible, and they are harder to detect and intercept. FSO also has electromagnetic immunity.
- *Compactness:* Small, lightweight, and compact design of the optical components ensures the system better follows SWaP limitations.
- *Cost:* Overall cost of the system is relatively low. Infrastructure cost is also much smaller as most of the FSO communication systems can be added as ad-hoc opportunistic networks complementing the existing radio technologies.
- *Power Consumption:* Power requirements can be managed as well based on applications. In general, power consumption is much lower for FSO systems compared to existing radio-based systems.

1.3 Challenges of FSO Communication and Viable Solutions

FSO communication does not come with advantages only, it has significant amount of challenges as well. Major challenges for FSO communication and their corresponding viable solutions are discussed here:

- *Additive Noise and Background Radiation:* One of the major challenges of FSO communication is management of additive noise and background radiation. Proper choice of sensitive detector with selective filters can ensure regeneration of signals at the receiver end.
- *Free Space Path Loss:* FSO links experience free space path loss due to multi-path dispersion and channel fading. Free space path loss results in limited link range for effective data

transmission. With adaptive signal modulation, power management, and sensitive detector can increase link range to acceptable range.

- *Atmospheric Losses:* Airborne particle and weather conditions, such as fog, rain, and smoke, can introduce additional atmospheric losses to the FSO link. Power control, mesh architecture, and hybrid RF/FSO systems can be implemented to mitigate the effect of atmospheric losses.

- *Atmospheric Turbulence:* Atmospheric turbulence causes FSO link failure as the optical beams are highly directional and narrow. Use of adaptive optics and spatial diversity can reduce the effect of atmospheric turbulence on the performance of FSO link.

- *Sway, Motion, and Vibration:* Mobile platforms are prone to link failure due to vibration and sway misalignment of the transmitters and receivers. Robust and fast tracking system needs to be incorporated to eliminate the effect of motion on the link up-time. Also, smart optical design can be implemented to address the issue of drift while two mobile nodes are in the process of communicating.

The comparison of FSO systems over RF and fiber-based systems are shown in Table 1.1. It is evident that RF-based systems can provide mobility for shorter span in indoor and outdoor settings, however data rates that are available to end users are much higher for FSO-based systems. This max throughput capability makes it easier to implement FSO as the last-mile solution to the high demand issues. Fiber-based systems provide the backbone of the high-speed systems, but existing RF systems are the bottleneck for delivering the high-speed data to the end users. Even though FSO enables high mobility and secure connectivity, FSO experiences sensitivity to external conditions which limits the link range and application diversity.

Technology	RF Network	Fiber-based Network	FSO Network
Max Throughput	a few Gb/s	>10 Gb/s	>10 Gb/s
Mobility	Yes	No	Yes, but limited
Cost	Low	High	Low
Infrastructure	No	Yes	No
Interception	Yes	With difficulty	With difficulty
Specific Frequency Band	Yes	No	No
Sensitivity to External Condition	No	No	Yes

Table 1.1: Comparison Table for RF, Fiber, and FSO systems

1.4 FSO Network Classifications

Depending on the applications and link range variations, FSO networks can be classified into three (3) major categories, as shown in Fig. 1.2:

1. Optical Wireless Satellite Networks (OWSNs)
2. Optical Wireless Terrestrial Networks (OWTNs)
3. Optical Wireless Home Networks (OWHNs)

The comparative applications of the FSO network classifications are given in Table 1.2. It is clear from the table that FSO can be implemented in various applications based on the the hardware requirements and performance limiting factors. In this thesis, our efforts relate mostly to the OWHNs (IrDA) applications of the FSO network. Even though IrDA standards were introduced for indoor applications in 1993, now-a-days it has shown potential for various short range outdoor applications as well. With proper design and hardware selection, IrDA systems can be used with autonomous vehicles, UAVs, and building-to-building communications. This particular sub-category provides a moderate FOV with portability for mobile applications.

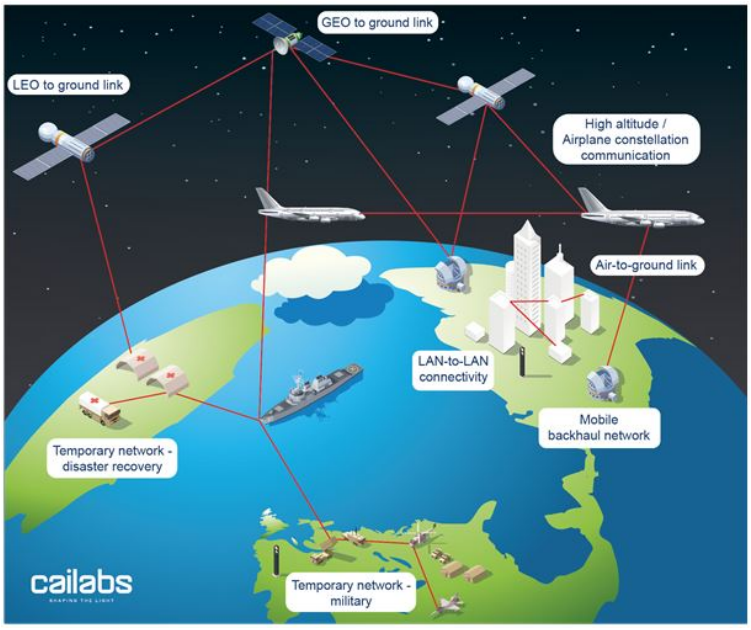

Figure 1.2: Classification of the FSO networks [ref: CaiLabs].

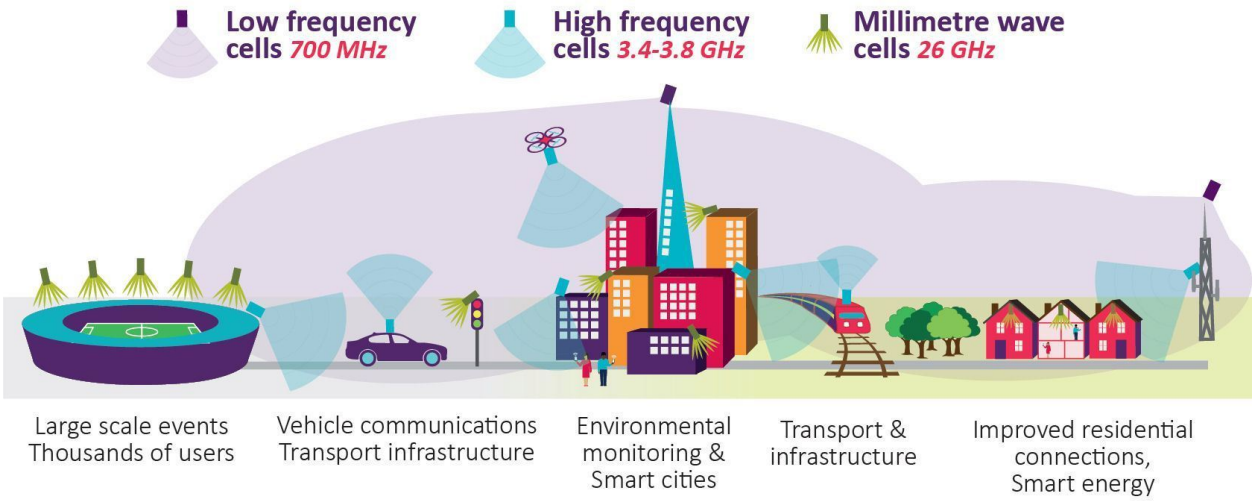

Figure 1.3: Recent trends of applications of OWHNs [Ref: cablefree.net].

	OWSNs	OWTNs	OWHNs (IrDA)	OWHNs (VLC)
Location	Orbit	High/Open Place	Indoor/Outdoor (Short range)	Indoor
Link Distance	∼84,000 km	∼10 km	∼Few meters	∼Few meters
Channel	Vacuum channel	Air turbulent channel	Weak turbulent channel	Weak turbulent channel
RX FOV	Very narrow	Narrow	30°	Wide
Performance Limiting Factor	Misalignment	Atmospheric turbulence	Limited power for eye safety	Limited power for eye safety
Hardware Requirement	Precise steering technology	Turbulent resistant design	Lightweight, portable, and inexpensive	Uniform diffuser
Misc.	Long distance coverage and expensive maintenance	Various impairment factors	Short-range point-to-point link	Exploiting reflection

Table 1.2: Comparison of FSO Network Categories [1].

The recent trends of the OWHN focuses mainly on short-range and low-elevations civilian applications, including mobile nodes, and can be classified into few major categories:

- Large scale events where thousands of attendees need connectivity
- Autonomous vehicle and vehicle monitoring pattern at busy locations
- Smart city and environmental monitoring
- Transportation infrastructure
- Indoor or residential connections through VLC

1.5 Mobile FSO System

Mobile Ad-Hoc Network (MANET) is a network of mobile platforms forming an autonomous connectivity without any access point. These mobile platforms or systems are very useful for many applications where no infrastructure is present or existing infrastructure is compromised due to natural disasters. Connecting the people of Puerto Rico during Hurricane Maria is a glowing example of the usefulness of Mobile FSO Networks. Surveying a remote location or performing an emergency procedure on a patient from a distance can be done using MANET protocols. Emerging technologies and high-speed devices are used to perform these tasks which is becoming more difficult to establish with existing RF networks due to increased demand for such telemetry applications.

Mobile FSO systems require short-range, robust, and reliable communication protocol. Designing and implementation of mobile FSO systems can be classified into four (4) steps:

1. *Channel Modeling:* A comprehensive channel model needs to be developed to calculate and incorporate free space path losses, atmospheric losses, atmospheric turbulence, and self-interference suppression model. This channel model will give a complete guideline to determine link range, power requirements, positioning optical elements, and optimize overall channel performance.

2. *System Design:* Based on the developed channel model, appropriate transmitters and receivers needs to selected to develop the system prototype. The several parameters that need to be considered to choose the optical elements include power levels, transmitter divergence angle, beam profiles, receiver FOV, and sensitivity.

3. *Pointing and Tracking (PAT) System:* PAT is one of the most important aspects of designing a mobile system. It requires both hardware and software direction to develop a PAT system.

Vibration model of the mobile platform needs to be considered to develop the PAT algorithm. Pointing can be controlled either by using hardware (single element, gimbal-based design) or software (multi-element, electrical steering-based design). PAT system needs to be time-synced with the data transmission unit by integrating it with the controller.

4. *Data Processing:* For full-duplex application, data thread management is also very important to ensure error-free communication. Synchronous data stream management, encoding the data at the transmitter end, decoding the data at the receiver end, and data storage management are important aspects of design challenges that needs to be addressed to achieve high-performing mobile FSO system.

1.6 Literature Review

In this section, we first present the existing literature on full-duplex RF communications. Then, we discuss some previous work that addressed the problem of full-duplex transceiver design for FSO communications. We will also include the weather-dependent performance studies and models proposed and how we can incorporate those models into design and performance estimation of in-band full-duplex optical wireless communication.

1.6.1 Full-duplex RF

The concept of designing full-duplex transceivers has been around since the 1940s, but recent requirement for higher bandwidth transmission ignited much interest in implementation of in-band full-duplex (IBFD) wireless communication systems [23, 24, 25]. By utilizing IBFD mode, the ergodic capacity can theoretically be doubled compared to the half-duplex mode [26]. Despite other advantages, such as reduced end-to-end delay and improved efficiency of ad-hoc network proto-

cols, IBFD design has few challenges as well, such as self-interference (SI), increased inter-node interference, and design complexity [24]. Self-interference cancellation (SIC) techniques for IBFD mode operation can be classified into active and passive schemes. For active SIC, analog cancellation is done in order to suppress SI before it enters the analog-to-digital converter (ADC) [24]. Active cancellation can be achieved in two ways: First, by injecting a replica transmit waveform into the receiver of the same transceiver using Balun transformer [27]; and second, by introducing path loss and delay in the digital domain, which cancels the SI when converted into analog and added with transmit signal [28]. For passive SIC, SI is suppressed even before entering receiver path [23]. This essentially means establishing an electromagnetic obstruction in the path of SI by using a directional antenna [28] or an absorbing material in the SI path [10].

1.6.2 Full-duplex FSO

Prior work on full-duplex FSO communication has reported transceiver designs using out-of-band techniques. Full-duplex indoor optical wireless communication is demonstrated for error-free ($BER < 10^{-9}$) short range operation [11, 12]. The transceiver used different optical wavelengths for uplink (1550.12 nm) and downlink (850 nm) channels, which makes it an out-of-band design. To suppress the SI for full-duplex mode operation, two separate bands are used for the transmitter and the receiver. Wang *et al.* [29] reported a full-duplex VLC system which implements subcarrier multiplexing (SCM) and wavelength division multiplexing (WDM) technique based on commercially available LEDs. Bit-error rate reported for 66 cm free-space delivery was 3.8×10^{-3}, but the use of RGB LEDs essentially makes the design out-of-band. To the best of our knowledge, the only in-band full-duplex design for FSO communication has been reported by Oh *et al.* [30], which implements communication between a stationary controller and a mobile node using beam reversibility and data erasure method. Even though this design implements full-duplex operation for the mobile node, the controller has only a transmitter but no receiver. Johnson *et al.* proposed

isolating the transmitter and the receiver of a node using a divider, but no functional prototype was demonstrated [14].

1.6.3 Turbulence Effect on FSO

Light has been source for communication since the beginning of civilization as lighthouse or signaling beacon, but foggy or rainy weather and atmospheric turbulence limited the extent of the communication. Due to the atmospheric and turbulence effect on free-space optical signals, advancement for optical wireless communication with promising solutions to the turbulence effects has been relatively new. In the last couple of decades, many statistical models have been proposed to characterize the optical wireless channel under turbulent weather [31, 32, 33, 34]. By implementing log-normal or gamma-gamma distribution of the irradiance in optical channel, performance of the link, such as average channel capacity and signal to noise ratio (SNR), have been estimated [35, 36]. However, those works focused on half-duplex configuration of the optical channel. In this work, we carry out weather-dependent performance analysis for in-band full-duplex optical wireless channel.

1.6.4 Directional Neighbor Discovery

Technology involving FSOC between unmanned aircrafts will connect areas of the world that currently do not have internet structures [37]. This kind of UAV based base-stations have garnered a wide attention due to several humanitarian crisis in recent years, such as hurricane Harvey and hurricane Maria in 2017. Facebook developed one drone-based internet service provider named project Aquila that can support date rate in Gbps [5]. A method of establishing FSO link with the aid of GPS, an out-of-band RF channel, camera, and communication with a base station at

ground are presented in couple of subsequent works [38, 39]. LOS alignment for these works were achieved initially by using GPS or camera to identify neighbor nodes; FSO channel was only used to transmit and receive data, not discovery or maintenance purpose. Unlike out-of-band technique, Khan *et al.* proposed an in-band method that determines LOS between hovering UAVs in 3D domain using FSO transceivers mounted on mechanically steerable heads [4].

Choudhury *et al.* designed a MAC protocol for ad-hoc networks with directional transmitters and omnidirectional receivers [40]. An *et al.* proposed a handshake based self adaptive neighbor discovery protocol, which also considers directional transmitters and omnidirectional receivers [41]. Ramanathan *et al.* proposed first directional full system design using directional antennas, along with GPS clock cycle synchronization [42]. Pei *et al.* proposed another neighbor discovery protocol for directional mobile ad-hoc networks (MANETs) based on synchronous search and positional information available from GPS [43]. Jakllari *et al.* proposed a polling based MAC protocol for MANETs using directional transmitters and receivers [44]. Khan *et al.* proposed a neighbor discovery algorithm considering omni-directional RF only to exchange orientation information and then searching for neighbors using FSO transceivers without using GPS [45]. Several mechanical beam steering approaches, such as MEMS-based mirror [46, 47], servo-based gimbal [3], liquid crystal modulators [48], and optical phased arrays [49], and optical beam steering approache, such as infra-red (IR) beam steering using lens system [50], can be adopted to establish LOS for mobile FSO networks[51]. In addition to the multi-element transceiver and mechanical beam steering techniques, a near-afocal lens assembly for the transmitter can provide tolerance to vibration and sway to ensure LOS [52].

1.6.5 Multi-Element Transceivers

To improve link quality and provide higher throughput, a large number of transmitters with directional propagation characteristics over same link can be deployed for FSOC, especially to achieve higher aggregated bandwidth and link robustness due to spatial diversity [53]. Bilgi *et al.* reported that FSO mobile ad-hoc networks (FSO-MANETs) can be designed using optical antennas in spherical shapes, which can achieve angular diversity, spatial reuse, and multi-element incorporation [54]. Alignment and mobility issues of multi-element FSO transceivers were analyzed and modeled by Kaadan *et al.* [55]. Also, in a similar fashion but with less focus on angular diversity, several issues on multi-element VLC systems are investigated by Eroğlu *et al.* [56, 57]. In these works, the authors investigated localization and tracking of users, LED assignments, and transmit power control for optimum operation. In a recent work, a Line-of-Sight (LOS) alignment protocol has been employed to tackle the hand-off issue caused by the mobility of the receivers in a room using multi-element VLC link by optimizing link performance [58]. In contrast, in our work, we focus on designing and *tiling multiple elements on a single transceiver plane* so that we can achieve the best performance out of the established FSO link in terms of robustness against mobility.

1.6.6 Laser-based FSOC System Applications

FSOC systems can be categorized based on optical link range and location of deployment. Short-range systems can be very useful for indoor applications and utilizes the wider divergence angle of LEDs to establish optical links. However, otdoor application requires more narrow beam transmitters and susceptibility to atmospheric turbulence and instability of the mobile platform. Desai *et al.* demonstrated a medium range FSOC system between stationary devices located 500 m to 5 km apart [59]. Furthermore, 72 Mbps to 2.88 Gbps datarate has been demonstrated for near-Earth communications using FSOC systems in the NASA project Laser Communications Relay

Demonstration [60]. Before shutting down the campaign in March 2021, the Google Project Loon provided internet to remote areas as a part of hurrican disaster relief by using a network of balloons at 20 km above sea level through long-range FSOC[61]. Recently, laser inter-satellite links between two LEO Starlink satellite has been reported and deployed which can be a crucial component is achieving low-latency communication paths for next generation satellite networks [62]. However, in this work we focus on short to medium range FSO links with limitations on size, weight, and power (SWaP) to achieve low-altitude laser links for massive network deployment.

1.7 Dissertation Overview

In this work, we emphasize on design and prototype of IBFD-FSO transceiver for aerial platforms. The major contributions of this work are listed here:

- We conducted a simulation study of the weather-limited performance between two IBFD transceivers by considering SI. We developed a model to interpret the effect of SI on the channel performance, which can be used for future channel modeling.

- We demonstrated proof-of-concept prototype of a short-range IBFD-FSO transceiver using off-the-shelf components using isolation mechanism. The prototype addresses different system issues such as threading, queuing, and storage of transmitted and received data-streams. The prototype successfully transmitted an image file in an IBFD manner, which can be reconstructed and displayed on the receiver end.

- The IBFD-FSO transceivers are mounted on aerial platforms (DJI M1000 Quad Drone) to establish a communication link between hovering aerial nodes. The transceivers successfully completed a three-way handshake to discover each other while hovering. To the best of our knowledge, no such prototype has been reported for IBFD-FSO transceiver for mobile setting.

- We explored different discovery algorithms to establish an LOS link between communicating nodes using IBFD-FSO transceivers. We implemented the prototype by mounting the IBFD-FSO transceivers on a mechanically steerable platform which can search in the 3D space for other communicating nodes within its communication range.

The rest of the report is organized as follows: A weather-limited channel performance analysis for IBFD FSOC is discussed in Chapter 2. A prototype of short-range IBFD FSO transceiver is demonstrated in Chapter 3. The asynchronous LOS discovery algorithm for a mechanically steerable platform implementing the prototype of IBFD transceiver is reported in Chapter 4. We discuss the design and optimum tiling of multi-element optical transceiver using genetic algorithm in Chapter 5. In Chapter 6, we propose a fixed effective focal length lens system with adjustable defocusing length to optimize the optical coupling efficiency and vibration tolerance for mobile FSOC links. Finally, we conclude with a summary of the progress thus far and a brief description of proposed research tasks.

CHAPTER 2: WEATHER-LIMITED IN-BAND FULL-DUPLEX TRANSCEIVER

Free-space optical (FSO) communication has gained popularity for wireless applications over legacy radio frequency for advantages like unlicensed operation, spatial reuse, and security[1]. Even though FSO communication can achieve high bit rates, range limitation due to strong attenuation and weather dependency has always restricted its practical applications to controlled settings such as building-to-building communication. Futuristic mobile and secure ad-hoc FSO network applications like smart cars and air-subsea links need more efficient and autonomous link acquisition capabilities which can be enabled by in-band full-duplex (IBFD) operation. IBFD-FSO transceivers will potentially increase network capacity significantly as well. In this work, we prototype an IBFD-FSO transceiver consisting of a VCSEL and a photodiode by addressing systems challenges, and model such transceivers to determine the range and weather dependent performance of the FSO link.

In this chapter, the main contributions are as follows:

- We model an IBFD-FSO transceiver having bandwidth of 175 MHz by using VCSEL as transmitter and Si PIN photodiode as receiver at 900 nm wavelength to determine the range and signal quality of the communication link. We incorporate atmospheric attenuation, surface reflection, and back-scattering to observe the weather dependency on the link performance. We consider the FSO beam propagation model and transmitter geometry for modeling as well as vary transmitter power and visibility range (100 m – 25 km). We find that for clear weather (e.g., visibility being 25 km) and 10 mW transmitter power, the IBFD-FSO communication link can range up to 120 m [64].

[1]This work was published in IEEE LANMAN 2018 [63]

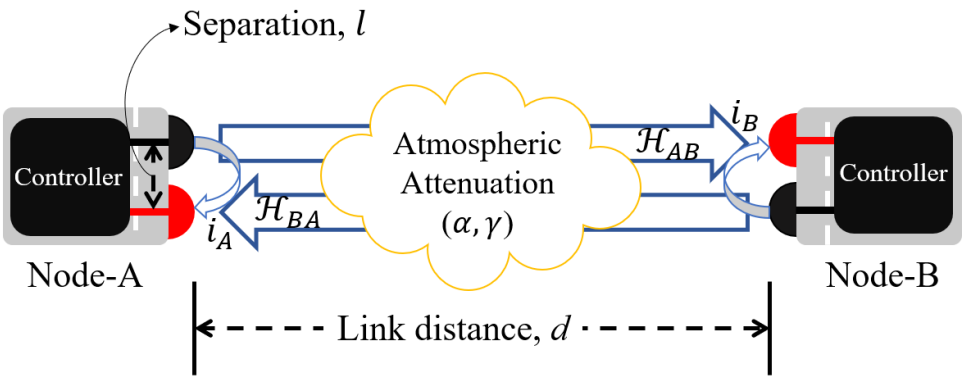

Figure 2.1: Block diagram of an in-band full-duplex optical wireless link consisting of two nodes.

- We calculate quality of the link in terms of signal-to-interference-plus-noise ratio (SINR) where visibility and transmitter power are taken into account.
- We propose an analytical model for self-interference cancellation due to the presence of an isolator within a transceiver unit.

2.1 Analytical Model of an IBFD FSO Link

To calculate signal-to-interference-plus-noise ratio (SINR) of an IBFD FSOC link, we have to consider overall atmospheric attenuation, noise margin, and self-interference signal. The block diagram of the system, having link length of d, is shown in Fig. 2.1. The separation distance of the transmitter and the receiver of each transceiver is denoted as l. Each node has a controller unit that handles data conversion, queuing and storage to operate in full-duplex configuration.

When two transceiver nodes communicate with each other in full-duplex configuration, both nodes transmit and receive optical signal simultaneously. Let us consider x_A and x_B are transmitted signals from nodes A and B respectively, while y_A and y_B represent received signals. If we denote additive

white Gaussian noise as w_A and w_B, then we can write the received signals as

$$y_A = \frac{1}{\sqrt{\alpha d^{\gamma}}} \mathscr{H}_{BA} x_B + w_A + i_A(P_A), \tag{2.1}$$

$$y_B = \frac{1}{\sqrt{\alpha d^{\gamma}}} \mathscr{H}_{AB} x_A + w_B + i_B(P_B), \tag{2.2}$$

where $\mathscr{H}_{AB}$ and $\mathscr{H}_{BA}$ represent channel impulse functions for the forward and reverse channels, respectively, and $i_A(P_A)$ and $i_B(P_B)$ are the residual SI signals at nodes. P_A and P_B are the transmitted signal powers at nodes A and B, respectively. Also, α is the FSO path loss attenuation coefficient, which we calculated for different visibility conditions in equation 2.7. In the equations 2.1–2.2, d is the distance between two nodes and and γ is the free-space path loss exponent of the channel. Typical value of γ for free-space propagation is 2, however the value can vary for urban areas in the range of 2.7 – 3.5 [65]. In this study, we set the value of γ to 2.

A mathematical formulation of the transmission link can be defined by calculating received power by incorporating weather-dependent atmospheric attenuation coefficient and noise components such as Rayleigh scattering, thermal radiation, and back reflection. A list of important symbols is given in Table 2.1.

2.1.1 Atmospheric Attenuation Coefficient

In this section, we will calculate the attenuation of optical signal over FSO channel. The optical signal, propagating through free-space medium, experiences different attenuation factors. The received power at the receiver end is given by Friis transmission equation [66]

$$P_R = P_T G_T G_R T_{atm} L_{FS}, \tag{2.3}$$

Table 2.1: List of symbols

Symbol	Description
L_{FS}	Free-space loss parameter
T_A	Atmospheric loss parameter
α	Atmospheric attenuation coefficient
γ	Free-space path loss exponent
d	Link distance
l	Separation between transmitter and receiver
V	Visibility
Γ_s	Residual self-interference (SI) power
β	Coefficient of SI suppression by separation
μ	Coefficient of SI suppression by isolation
δ	Exponent of SI suppression by isolation
N_T	Average noise equivalent power (NEP)

where P_T is the transmitted power, G_T and G_R are the transmitter and receiver gains, respectively, T_{atm} is atmospheric transmission coefficient, and L_{FS} is free-space loss parameter. Free-space loss parameter for omnidirectional transceiver is given by [66]

$$L_{FS} = \left(\frac{\lambda}{4\pi d}\right)^2, \tag{2.4}$$

where λ is the wavelength of transmitted signal and d is the link length. For our directional transceiver, we modified the free-space loss parameter using divergence angle (ϕ) of the transmitter [67]

$$L_{FS} = \frac{\lambda^2}{4\pi} \times \frac{A_R}{2\pi d^2(1-\cos\phi)}, \tag{2.5}$$

where A_R is the effective receiver area of the detector.

Attenuation of transmitted power through atmosphere is dependent on free-space loss and scatter-

ing loss, which can be modeled using exponential Beers-Lambert Law [68]

$$\tau(R) = \frac{P_R}{P_T} = e^{-\alpha d}, \tag{2.6}$$

where α is the attenuation coefficient (per unit length). By equating equation 2.6 to the P_R/P_T ratio from equation 2.3, we can calculate the attenuation coefficient as

$$\alpha = \frac{1}{d} \ln \frac{1}{G_T G_R T_{atm} L_{FS}}. \tag{2.7}$$

Again, the value of α depends on wavelength of the signal (λ), visibility range (V), and size distribution of the particle (q) in the atmosphere. The equation of atmospheric attenuation coefficient is proposed by Kim *et al.* [69] in the form of

$$\alpha = \frac{3.91}{V} \left(\frac{\lambda}{550 \text{ nm}} \right)^{-q}, \tag{2.8}$$

where q is given by

$$q = \begin{cases} 1.6; & V > 50 \text{ km} \\ 1.3; & 6 \text{ km} < V < 50 \text{ km} \\ 0.72V^{\frac{1}{3}}; & V < 6 \text{ km}. \end{cases} \tag{2.9}$$

By comparing equations 2.7 and 2.8, we can calculate the gain product $G_T G_R$. We can use this product term to calculate the received power (P_R) for any given transmitted power (P_T) using equation 2.3.

2.1.2 Noise Calculation

The variance in the current noise when an optical signal is received by the detector is given by

$$\sigma_N^2 = \sigma_{\text{th}}^2 + \sigma_{\text{B}}^2 + \sigma_{\text{dark}}^2 + \sigma_{\text{T}}^2, \tag{2.10}$$

where σ_{th}^2, σ_{B}^2, σ_{dark}^2, and σ_{T}^2 are noise variance in current due to Johnson (thermal) noise, background radiation, dark current, and transmitted signal, respectively [70, 71, 72]. Noise equivalent power (NEP) is defined as the quantitative measure of the sensitivity of a detector or the power generated by a source of noise on a detector [73]. The equations for the NEP of the optical components are given by [74]

$$P_{bg\_sn} = \frac{\sqrt{2qSP_{bg}B_{en}F}}{S}, \tag{2.11}$$

$$P_{sig\_sn} = \frac{\sqrt{2qSP_{sig}B_{en}F}}{S}, \tag{2.12}$$

$$P_{dark\_sn} = \frac{\sqrt{\left(2qI_{dark}G_{det}^2F + 2qI_{dc}\right)B_{en}}}{SG_{det}}, \tag{2.13}$$

where P_{bg} is the optical solar background noise, P_{sig} is the optical power of the signal, I_{dark} is optical dark current, I_{dc} is the dc dark current, G_{det} is the detector current gain, B_{en} is effective noise bandwidth ($= \frac{\pi B}{2}$), S is radiant sensitivity of the detector (amp/watt), F is excess noise factor which is equal to 1 for photodiode, and q is the electronic charge. The total NEP is given by

$$N_T = \sqrt{P_{bg\_sn}^2 + P_{sig\_sn}^2 + P_{dark\_sn}^2}. \tag{2.14}$$

To design a short-range FSOC system using laser as transmitter, all the noise contributions need

to be incorporated in calculation. As the bit-rate requirement is increasing day-by-day, receiver components and circuit are required to be very sensitive and responsive. With the increase of sensitivity, receiver noise budget is becoming smaller.

2.1.3 Residual Self-Interference Model

By using the residual SI model of [75, 76], residual SI power at nodes A and B are given by

$$\Gamma_{sA} = \frac{P_A^{1-\delta}}{\beta\mu^{\delta}} \quad \text{and} \quad \Gamma_{sB} = \frac{P_B^{1-\delta}}{\beta\mu^{\delta}}, \tag{2.15}$$

where β represents the coefficient of SIC by separation of the transmitter and the receiver within the same transceiver unit, and μ and δ represent SI suppression parameters for deployed passive SI cancellation technique. P_A and P_B are the transmitted signal power at nodes A and B, respectively.

Within a transceiver unit, the distance between transmitter and receiver is denoted as l and the coefficient of passive SIC coefficient is μ. The exponent of passive SIC is denoted as δ, which can be between any value from 0 to ∞. The case $\delta = 0$ represents when there is no passive SIC is implemented, whereas $\delta = \infty$ represents perfect cancellation of SI. Again, $\delta = 1$ means there is a constant residual SI power present irrespective of the transmit power, which portraits an unrealistic scenario for full-duplex application. However, there is threshold value of δ for which full-duplex performance supercedes the performance of half-duplex operation, which can be defined as δ^*. The typical values for δ^* lies between 0.6 to 0.8 [76]. Usually it can can be defined that any value of δ that is less than δ^* represents low SIC and higher δ value represents high SIC region. For this study, we will consider $\delta = 0.2$ for low SIC and $\delta = 1.8$ for high SIC performance.

The value of the coefficient of SIC by separation, β, depends on the distance (l) of the transmitter and receiver within a transceiver unit and the free space attenuation coefficient. The equation can

be defined as

$$\beta = \alpha_{\perp} l^{\gamma}, \tag{2.16}$$

where $\alpha_{\perp}$ is the free space attenuation coefficient along the perpendicular direction of beam propagation and γ is the free space path loss exponent. Considering $l \ll d$ and comparatively higher divergence angle (θ) of the VCSEL, the value of $\alpha_{\perp}$ will be comparable to the value of the free space attenuation coefficient (α) for our system. For this study, we will consider $\alpha_{\perp} \approx \alpha$ and $\gamma = 2$.

2.1.4 SINR *Calculation*

In the previous sections, we have shown the formulation of free-space atmospheric attenuation, noise components, and residual SI. Let us consider a system consisting of two transceiver nodes, each having one transmitter and one receiver. Using these equations, SINR can be written for a transceiver with the transmitter having θ divergence angle and the receiver with detection area of A_{det} as

$$SINR_A = \frac{P_B T_{atm}(V) \lambda^2 A_{det}}{8\pi^2 d^2 (1-\cos\theta)\,(N_{TA} + \Gamma_{sA})}, \tag{2.17}$$

$$SINR_B = \frac{P_A T_{atm}(V) \lambda^2 A_{det}}{8\pi^2 d^2 (1-\cos\theta)\,(N_{TB} + \Gamma_{sB})}, \tag{2.18}$$

where N_{TA} and N_{TB} denote NEP at node A and B, respectively.

2.2 Simulation Results and Discussion

In this section, we will present our simulation results for the performance of an IBFD transceiver for different weather conditions and SI suppression parameters. We will evaluate free-space atmo-

spheric loss coefficient and corresponding link length for different visibility range. Then, we will evaluate SINR for different system parameters and transmitted power levels.

2.2.1 Attenuation Coefficient and Link Length

To calculate the atmospheric attenuation coefficient of the free-space optical signal, we implemented equation 2.6 using parameters of the system components at $\lambda = 900$ nm. We used detector parameters such as receiver area ($A_R = 1$ cm^2), and transmitter parameters such as divergence angle ($\theta = 24°$), to calculate free-space loss parameter, L_{FS}. We acquired atmospheric loss coefficient, T_{atm} from MODTRAN® simulation for different visibility ranges. MODTRAN® simulation parameters are listed in Table 2.2. We calculated atmospheric attenuation coefficient, α, using equations 2.3 – 2.6. The calculated α and corresponding link distance, L, are shown in Fig. 2.2. It can be seen from the figure that link distance is about 127 m when visibility is 1 km. With the increase of visibility, link distance also increases as we can observe from the figure, however it

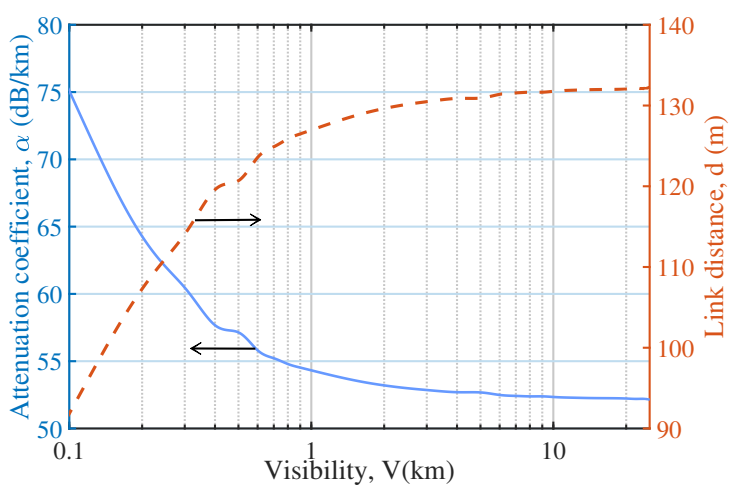

Figure 2.2: Attenuation coefficient and link distance variation with visibility using system parameters.

tends to plateau around 132 m.

Table 2.2: MODTRAN® simulation parameters

Item	Value/Description	Unit
Atmospheric model	Mid-latitude winter model	
Water	1059.7	atm-cm
Ozone	0.37681	atm-cm
CO_2	410	ppmv
CO	0.15	ppmv
CH_4	1.8	ppmv
Temperature	300	K
Aerosol model	Urban	

Attenuation coefficient due to free-space optical loss is highly dependent on the visibility of the atmosphere. By using the model described by Kim *et al.* [69], we can estimate the attenuation coefficient and corresponding permissible link distance as well. It can be noted from equation 2.8 that path loss exponent depends on visibility only, as a result the model over-estimates the link distance for higher visibility region. However, from the fitting model described in equation 2.8 we can estimate that compared to $1,550$ nm wavelength, signal at 900 nm experiences smaller attenuation coefficient, and hence, attains higher link distance. We also calculated attenuation coefficient for different wavelengths. As we can observe from Fig. 2.3, smaller wavelength and higher visibility lead to smaller attenuation coefficient.

2.2.2 Behavior of SINR

To evaluate SINR in the FSO channel, we considered two nodes, A and B, established communication in full-duplex manner. For this set of simulations, we set one transmitter and one receiver in each transceiver module, separated by a distance of $l = 5$ cm. We presented the model for SINR_A

and SINR_B in equations 2.17 and 2.18, respectively. We calculated SI suppression by separation coefficient, β, by using the equation 2.16. The value of β depends on the separation distance (l) and positions of the transmitter and the receiver in the same transceiver unit. Whereas, the value of the SI suppression by passive isolation coefficient, μ, represents the level of SI reduction when passive SI suppression technique is implemented. We set $\mu = 10$ dB to constant value for our simulations [75]. SI suppression by isolation exponent, δ, is varied to determine residual SI power at the receiver. The average NEP power, N_T, is calculated based on the formulation presented in the previous section.

Level of SI suppression is calculated while we set δ for different visibility ranges. As shown in Fig. 2.4, SINR for a node changes depending on δ values. The SINR value is calculated by using equation 2.17 for different δ values. We can see from the figure that as SIC level gets stronger (larger δ), performance of the channel gets better. Again, the value of SINR is strongly dependent on the atmospheric attenuation, hence with the increase of visibility and by comparing the value of attenuation level from Fig. 2.2, we clearly see improvement in channel performance as visibility

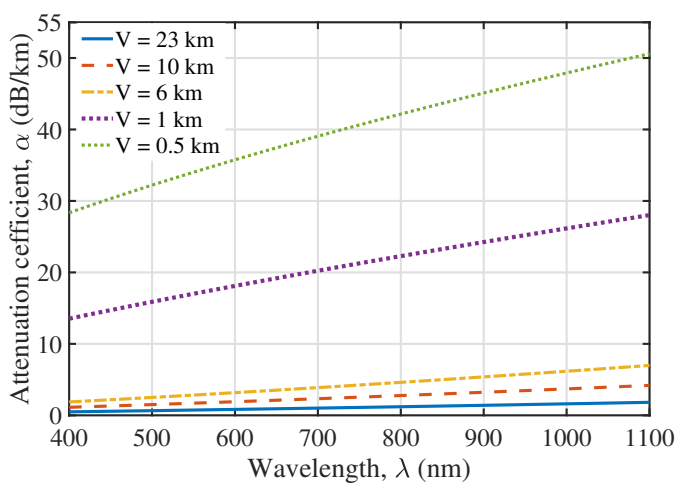

Figure 2.3: Attenuation coefficient variation with wavelength.

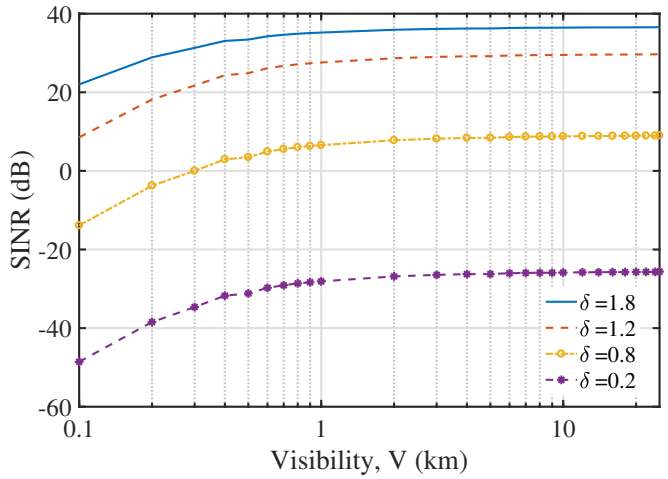

Figure 2.4: SINR variation for different visibility range.

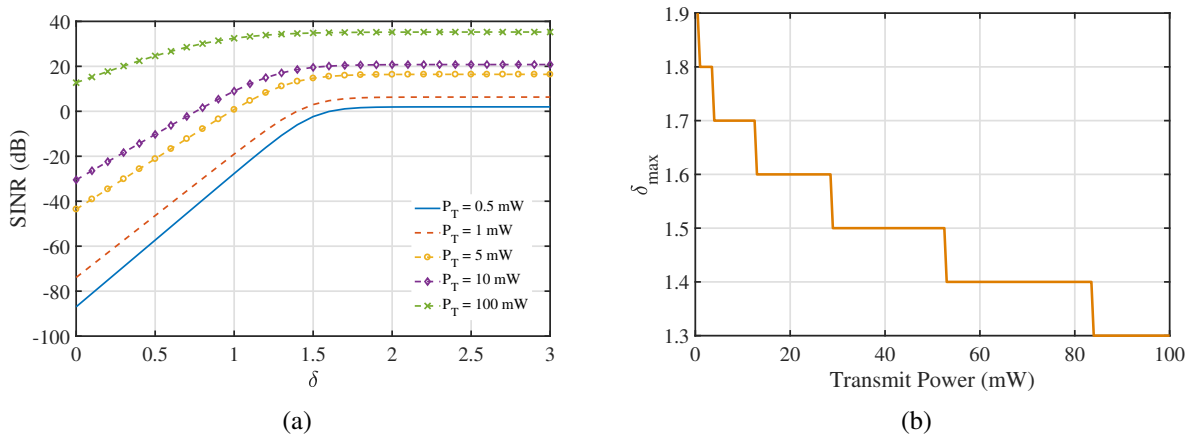

Figure 2.5: (a) SINR variation at different transmit power level with the change of δ, (b) SINR variation at node B for different visibility conditions and transmit power.

range (V) increases.

Figure 2.5(a) shows the SINR behavior for different δ under different transmit power levels. As δ increases and level of SIC improves, and SINR performance gets better. For smaller δ values, SIC suppression is weak and SINR is mostly dominated by NEP present in the system. We can

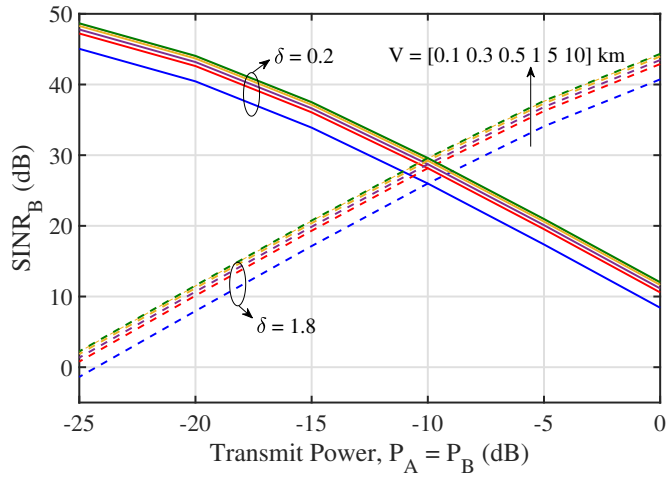

Figure 2.6: SINR variation at node B for different visibility conditions and transmit power.

see from Fig. 2.5(a) that SINR becomes constant after a level of SI suppression, because residual SI signal becomes too weak compared to AWGN signal present in the channel that any further improvement in active SI suppression does not help improving the performance of the transceiver. We also calculated δ_{max} which can be defined as the maximum value of δ for which the SINR of the link gets saturated for different transmit power levels. We can observe the declining trend of required δ_{max} with the increase of transmit power in Fig. 2.5(b). The optimum value of the exponent δ can be calculated from the model presented in this work.

Figure 2.6 indicates when both nodes are transmitting at the same power level, SINR improves with increase of visibility. As the value of β depends on transmit power, β needs to be recalculated for each transmit power level. We also showed SINR variation for $\delta = 0.2$ and $\delta = 1.8$, while both nodes transmitting same power, in Fig. 2.6. For the weak SI suppression ($\delta = 0.2$) case, SINR decreases with increase of transmission power. Because with weak SI suppression, residual SI signal increases with the increase of transit power. On the other hand, for strong SI suppression ($\delta = 1.8$), SINR improves with higher transmission power.

In summary, we have presented a comprehensive weather dependent channel model for in-band full-duplex optical transceivers by including atmospheric attenuation under various weather conditions. We developed a mathematical model for passive SIC by isolation technique. This model can be used to estimate the expected channel performance and provides a guideline for selecting optical elements for the FSO communication prototype.

CHAPTER 3: IN-BAND FULL-DUPLEX FSO TRANSCEIVER PROTOTYPE

In this chapter, we demonstrate a proof-of-concept prototype of a short range in-band full-duplex FSO transceiver built using off-the-shelf components[1]. We used the method of isolation to prevent the receiver of a node from receiving its own transmitted signal. We covered the transmitter and the receiver on all sides keeping only a small opening at the front. We conducted real test-bed experiments using our prototype to show its effectiveness in preventing self-interference or optical feedback. The results demonstrate that, isolating the transmitter and receiver of a node, optical feedback can be effectively stopped and in-band full-duplex communication can be realized.

3.1 FSO Transceiver Design

In this section, we discuss the issues related to designing in-band full-duplex free-space-optical (IBFD-FSO) transceivers.

The essential components of an IBFD-FSO transceiver (Figure 3.1) are as follows:

1. **Transmitter:** It is the source of signal which can be implemented by LEDs or lasers. Lasers have much narrower spectral width compared to LEDs. However, for short range communication, LED is preferable due to low cost, power efficiency and compact design. For long-range communication, laser gives better performance due to high directionality, high intensity, and high bit rate. A transmitter (T_x) also includes driver circuit, T_x buffer to store digital transmit data and an digital-to-analog (DAC) converter to convert digital data into

[1]This work was published in IEEE LANMAN 2018[77]

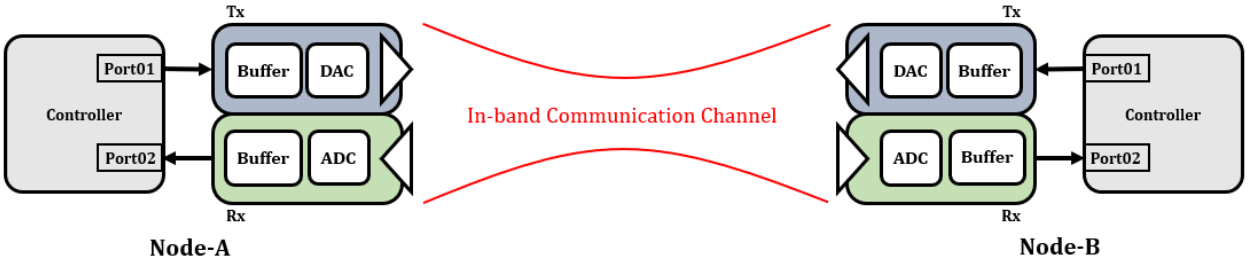

Figure 3.1: Block diagram of an IBFD-FSO communication system

analog signal.

2. **Receiver:** Receiver (R_x) circuit consists of either photo-diode (PD) or photo-resistor to capture incoming signal. PD can be fabricated using semiconductor material or charge coupled device (CCD) sensor. For in-band operation, detector bandwidth needs to be narrow and matched with transmitter signal bandwidth. Receiver also houses an analog-to-digital (ADC) converter and an R_x buffer to store inbound serial signal stream.

3. **Controller:** A central processing unit for controlling the transmitter, receiver and the overall operation of the IBFD-FSO communication system. Controller manages transmit and received data with proper threading and clocking. Two major properties that define an IBFD-FSO transceiver are to perform data transmission and reception: (i) simultaneously, and (ii) over the same frequency band. These are two important design issues that need to be addressed.

The two major properties that define an IBFD-FSO transceiver are to perform data transmission and reception: (i) simultaneously, and (ii) over the same frequency band. These are two important design issues that need to be addressed.

3.1.1 Simultaneous communication

An IBFD-FSO transceiver must be able to transmit and receive at the same time. So, the controller unit should be capable of controlling the transmitter and the receiver in parallel. This can be achieved by using separate threads for transmission and reception. To handle both transmission and reception simultaneously, two separate data-path and storage needs to be available to avoid SI in the processing unit. This can be done by availing two ports of the controller and using individual buffers for transmitter and receiver.

3.1.2 In-band communication

In-band communication refers to the idea of performing transmission and reception using the same free-space-optical channel (Figure 3.1). And this gives rise to the problem of optical-feedback or self-interference, where the signal transmitted by a node interferes with the signal at the receiver. So, another important design issue for developing an IBFD-FSO transceiver is: preventing optical feedback.

3.1.3 Optical feedback prevention

IBFD-FSO transceivers are designed to transmit in a single direction. But, similar to any electromagnetic source, the light source of the transmitter has a back-lobe and side-lobes in addition to the highly directional main-lobe, where the auxiliary lobes are weaker than the main-lobe [78, 79, 80, 81]. When the transmitter and the receiver are placed close to each other, these auxiliary lobes and optical reflections cause a node to receive its own transmitted signal. This is known as optical feedback or self-interference (SI). Preventing optical feedback is relatively easier to implement in an FSO transceiver compared to an RF antenna by inserting an optically obscure

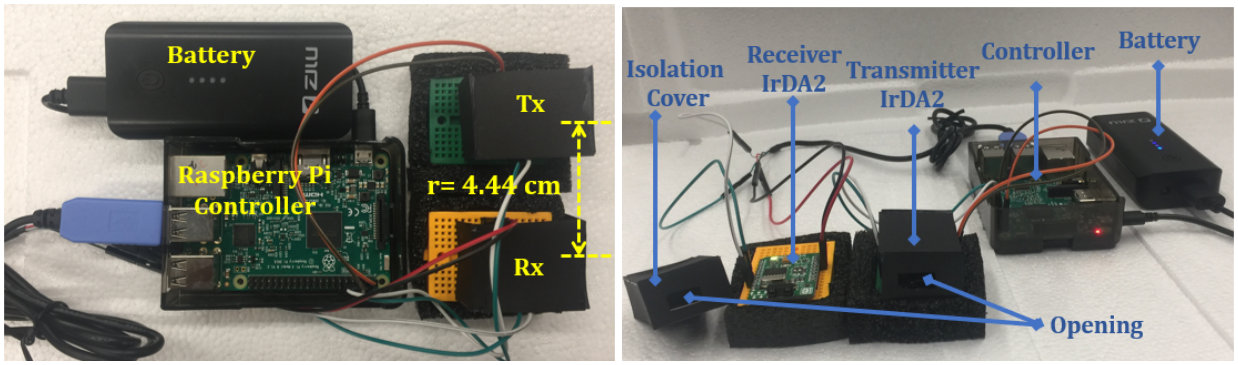

(a) Top view

(b) Front view

Figure 3.2: IBFD-FSO prototype

separator between transmitter and receiver. This can be accomplished by covering both the transmitter and the receiver individually on all five sides, except the front, where a pinhole opening allows signal transmission and reception respectively. The advantage of this isolation technique is two-fold: First, it either reduces or completely blocks the optical feedback, and second, it enhances the directionality of the transceiver.

3.2 Proof-of-concept prototype

We designed and built a prototype of the IBFD-FSO transceiver by utilizing commercially available off-the-shelf hardware and electronic components. The prototype is displayed in Figure 3.2. The main parts of the prototype are: A Raspberry Pi [82] as the controller and two IrDA2 Clicks [83], one of which is used as a transmitter and the other as a receiver. The IrDA2 Clicks are controlled by the Raspberry Pi using two separate threads: T_x thread and R_x thread.

3.2.1 IBFD-FSO controller

We used a Raspberry Pi 3 Model B as the controller, which is a single board computer (Figure 3.2). It has a Quad Core 1.2 GHz Broadcom BCM2837 64 bit CPU, 1 GB RAM, BCM43438 wireless LAN and 4 USB-2 ports. The details of these and other specifications are available in [82].

3.2.2 Transceiver

We used a combination of two IrDA2 Clicks [83]: One as the transmitter and another as the receiver. The IrDA2 Click consists of an infrared transceiver module compliant with the latest IrDA physical layer standard for fast infrared data communication. It supports IrDA speeds up to 115.2 Kbit/s. Integrated within the transceiver module are a photo pin diode, an infrared emitter (IRED). This device covers the full IrDA range of ≈ 2.75 m using the internal intensity control. The IRED has peak emission wavelength of 900 nm and its angle of half intensity is $\pm 24^o$. The IrDA2 Click board also features the MCP2120 which is a low-cost, high performance, fully-static infrared encoder/decoder. This device sits between a UART (Universal Asynchronous Receiver-Transmitter) and an infrared (IR) optical transceiver.

3.2.3 In-band full-duplex operation

The Raspberry Pi has one UART, to which we connected one of the IrDA2 Clicks: this was our transmitter. We used a USB-to-UART converter to connect the other IrDA2 Click to the Pi: this was our receiver. The setup is shown in Figure 3.2. Although the IrDA2 Click has both a transmitter and a receiver, it operates only in half-duplex mode. So, we used two separate IrDA2s, one of them only for transmission and the other for reception. We prepared two isolating covers, as shown in Figure 3.2 for the transmitter and the receiver. We used black cardstock papers for building the

Algorithm 1 IBFD-FSO Communication Threads

```
{Initialize the global variables}
R_x = TRUE //Start reception?
T_x = TRUE //Start transmission?
```

{Receives until an empty packet, writes the received data to a file}

Receive()

```
Local variable r.packet //Buffer of 115.2Kb
while R_x = TRUE do
    r.packet ← store received packet
    if r.packet ≠ NULL then
        write r.packet to file
    else
        R_x = FALSE
    end if
end while
```

{Reads from a given file until the end and transmits it}

Transmit()

```
Local variable t.packet //Buffer of 115.2Kb
while T_x = TRUE do
    t.packet ← read packet from file
    if t.packet ≠ EOF then
        send t.packet
    else
        T_x = FALSE
    end if
end while
```

covers. The cover has only an opening at the front for transmission and reception of signal. All the other sides are blocked for preventing optical feedback as was described in Section 3.1.3. We used Python [84] as the programming language for implementing the IBFD controller. The main program consists of two separate threads: T_x thread for operating data transmission and R_x thread for receiving, processing and storing the incoming stream of data. The pseudocode of the program is provided in Alg. 1.

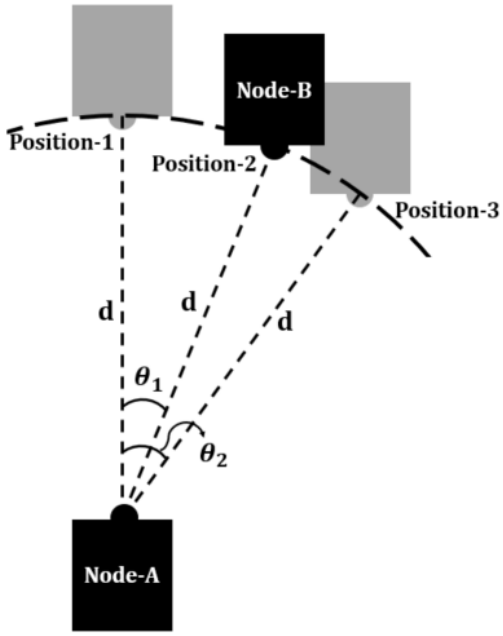

Figure 3.3: Experimental setup for finding throughput and packet-error-rate

(a) Test image file (b) Without isolation (c) With isolation (d) With surface reflection

Figure 3.4: Transmitted and reconstructed received image

3.3 Experiments and Results

We performed real test-bed experiments to gain insight about the effectiveness of the IBFD-FSO transceiver in preventing optical feedback. We used two identical nodes (A and B) with IBFD-FSO

transceivers for point-to-point communication. Figure 3.4(a) shows the image file transmitted between the transceivers during the experiments. The size of this file was 20.1 KBytes. We extracted the RGB pixel intensity values of the image file and created a separate text file of size 755.4 KBytes. On both nodes A and B, this text file was used for transmission. The Raspberry Pis on both nodes were controlled from a laptop via a secure shell session (SSH) over Wi-Fi. The laptop and the Pis were all on the same local-area-network (LAN). A simple three-way handshake through the Wi-Fi helped in synchronizing the simultaneous operation the two nodes. After the synchronization, both nodes started listening through their respective IrDA2 receiver. A small delay of (one second for node A and two seconds for node B) was added before starting the transmission operation on both nodes. This was done to make sure that a node did not start transmitting before the other one was ready to receive data. The different experiments that we conducted using the IBFD-FSO transceivers are described below along with the observed results.

3.3.1 Throughput and Packet-Error-Rate

First, we performed experiments without using the covers on the transmitters and receivers on both node A and node B. The transmitter and the receiver of a node was kept 0.044 m apart 3.2(a). The experiment was done on a table with black surface to prevent reflection. The nodes were kept facing each other at a distance of 1 m. The packet error-rates at both nodes were more than 90% because of optical feedback. The received image file is displayed in Figure 3.4(b) after reconstruction. We replaced the garbled pixel values with zeros. We conducted the rest of the experiments isolating the transmitter and the receiver of each node as described in Section 3.2.3.

We performed experiments using the setup shown Figure 3.3. We kept node A at a fixed position and changed the distance and angle of node B with respect to node A. We ran the experiments for different combinations of the distance between the nodes, $d = 0.5$ m, 1 m, 1.5 m, 2 m, 2.5 m, 2.75

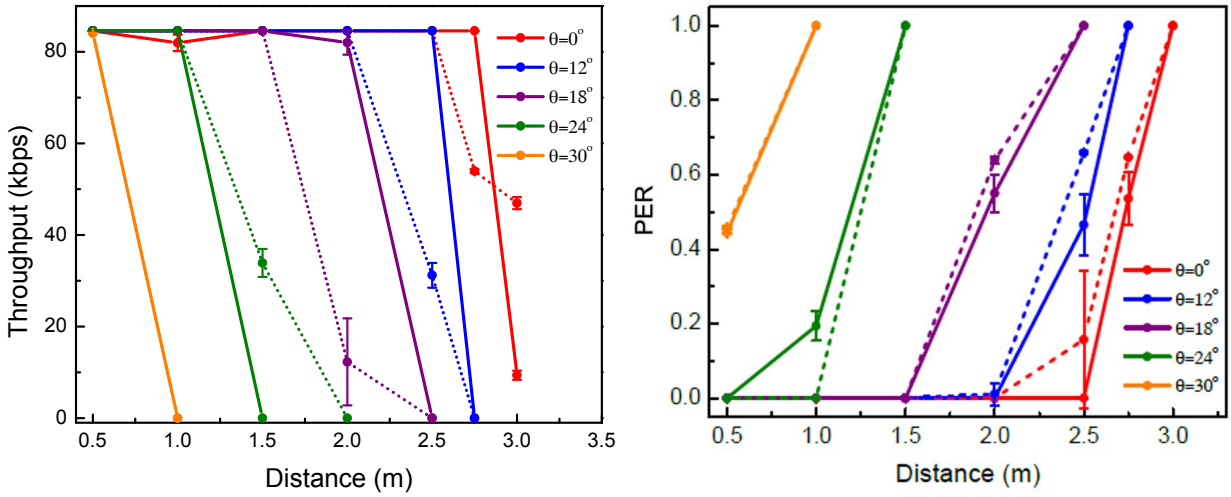

(a) Throughput: node-A(solid) and node-B(dashed)

(b) PER: node-A(solid) and node-B(dashed))

Figure 3.5: Performance of IBFD-FSO transceiver

m and 3 m, and angle, $\theta = 0^o, 12^o, 18^o, 24^o$ and 30°. Node A transmitted the text file extracted from the image file to node B. At the same time, node B transmitted a text file extracted from the same image file to node A. The size of the text file was 755.4 KBytes and transmission rate was 115.2 Kbps at both nodes. The experiment was repeated 6 times for each combination of d and θ. A correctly received reconstructed image is shown in Figure 3.4(c).

Figure 3.5(a) demonstrates the throughput achieved at both node A and node B. The solid lines represent the throughput values at node A, and the dashed lines represent node B's throughput values. We can see that, when the nodes were at an angle of $\theta = 0^o$ with respect to each other, the throughput was $\approx$ 84.5 Kbps up to a distance of $d = 2.75$ m at node A and up to $d = 2.5$ m at node B. For $d \geq 3$ m, the throughput values dropped significantly. When θ was increased to 12°, we can observe that the throughput drops below 84.5 Kbps for shorter distance between the nodes. We can see that, as θ is increased, the throughputs drops to values smaller than 84.5 Kbps for lower distances. The whole files were received at both nodes as long as they were within each other's region of coverage, i.e., $d \approxeq 3$ m and $\theta = 24^o$.

In Figure 3.5(b), the packet-error-rates (PERs) of the received files are displayed. Again, the solid lines represent node A's PER and the dashed lines show node B's PER. We can observe that, for both nodes, the BERs are very low ($\approxeq 0$) up to $d = 2.5$ m for $\theta = 0^o$, up to $d = 2$ m for $\theta = 12^o$, up to $d = 2.5$ m for $\theta = 0^o$ and up to $d = 1.5$ m for $\theta = 18^o$. Also, for $\theta = 24^o$, BER$\approxeq 0$ up to $d = 0.5$ m at node A and up to $d = 1$ m at node B. At both nodes, no effect of optical feedback was observed. The files were received correctly as long as the nodes were within the coverage area of each other.

We repeated the experiment 3 times for $d = 1$ m and $\theta = 0^o$ by changing the distance between the transmitter and receiver of a node to 1.9 cm. In this case also, the text files were correctly received at both nodes with almost 0% PER. Next, we placed the transmitter on top of the receiver at a height of 3.2 cm and repeated the experiment. We also performed experiments by placing the receiver on top of the receiver. In all these scenarios, the text files were transferred with almost no error.

3.3.2 Optical feedback by reflection from surface

As mentioned earlier, the results presented so far were achieved by performing experiments on a black surface to prevent reflection from the surface. In this section, we demonstrate results achieved by using a white surface. Figure 3.6 displays the experimental setup. We kept the nodes at distance of $d = 1$ m and at angle $\theta = 0^o$ with respect to each other. We placed a letter sized white paper between nodes A and B. We placed the white paper at different distances ($l = 6.25$ cm, 7.5 cm, 8 cm, 9.375 cm, 12.5 cm, 25 cm, 50 cm) from node A. We repeated the experiment twice for each value of l. We can see from Figure 3.7(a) that PER was almost 100% up to $l = 7.5$ cm. Figure 3.4(d) shows the received image after reconstruction at node A for $l = 7.5$ cm. Again, the garbled pixel values were replaced by zero. For longer distances, the file was correctly received

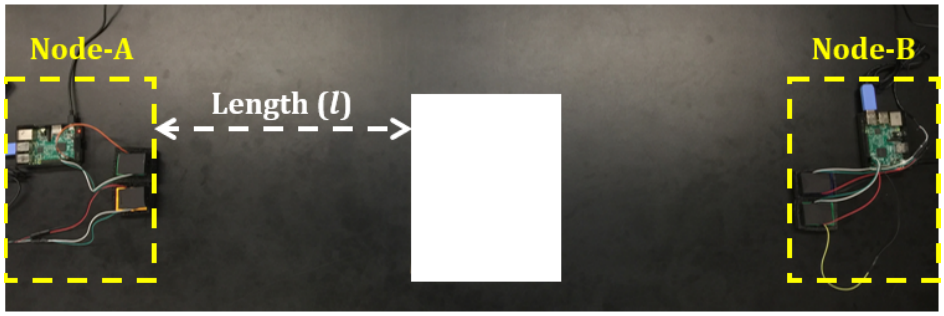

Figure 3.6: Experimental setup to evaluate reflection from the surface

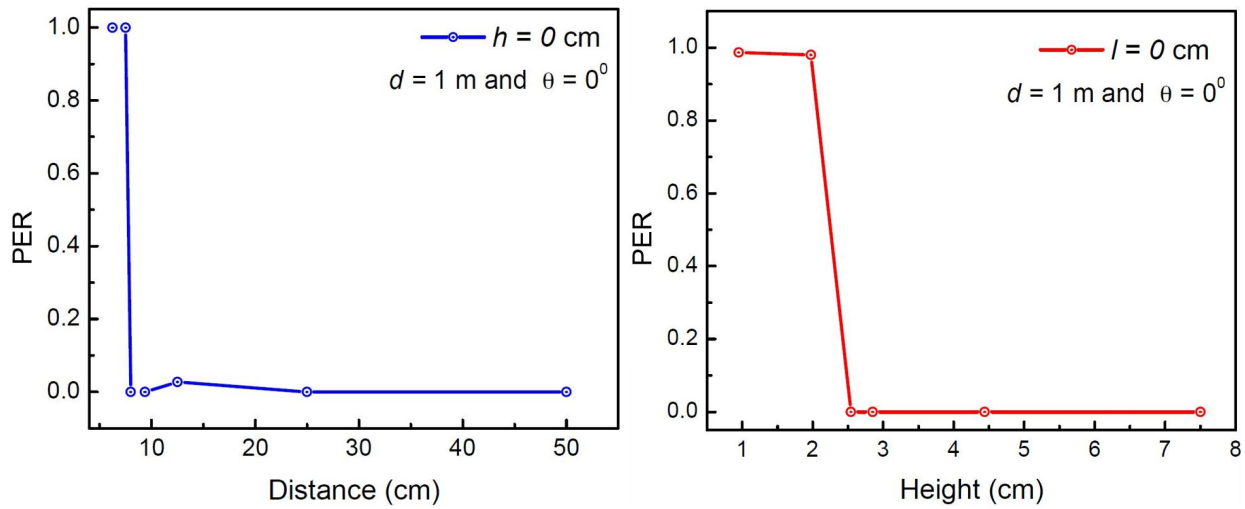

(a) PER vs. l

(b) PER vs. h

Figure 3.7: Optial feedback caused by reflection from the surface at Node A

every time.

We conducted further experiments by placing the white paper at $l = 0$ cm from node A. This time, we varied the height h of the transceiver from the surface. We observed that, for $h \leq 1.975$ cm, the BER was almost 100%. For higher values of h, there was no optical feedback caused by reflection from the white surface. We can see that, reflection from a non-black surface can cause optical feedback. But the experimental results show that, this can be prevented by placing the transceiver

at a proper height from the reflecting surface.

In summary, we presented a proof-of-concept prototype of an in-band full-duplex optical transceiver by implementing isolation technique to prevent optical feedback and self-interference. We used commercially available off-the-shelf components to design and build our prototype which limits the data transfer rate and link range of the communication channel. To increase the performance parameters, such as bit-rate and link range, custom designed components can be utilized. Furthermore, the overall SINR performance and self-interference suppression can be improved by implementing smart tiling design and improved active and passive isolation techniques.

CHAPTER 4: ASYNCHRONOUS LOS DISCOVERY ALGORITHM USING IBFD FSO TRANSCEIVERS FOR AERIAL NODES

FSO-enabled UAVs are envisioned to play a significant role in future generation mobile wireless ad hoc networks. Swarms of UAVs connected to each other via FSOC links can help to relay data from pico-cells to the core network[1]. UAVs are also used for both civil and military missions, such as monitoring of an area hit by a natural disaster, broadcasting data at some critical sports event or even observing behind the enemy lines. Recently, Alphabet Inc. deployed stratospheric solar-powered balloons to provide Internet service to remote areas of Puerto Rico where cellphone towers were damaged by Hurricane Maria. All these different applications of UAVs produce large amounts of data that is required to be delivered to a ground station or other UAVs [17]. Using FSO transceivers, these large volumes of data can be transferred at extremely high speeds.

In this work, we tackle the problem of LOS link discovery using directional FSOC links between nodes in 3D space. We assume that the nodes can mechanically steer their respective transceivers with randomly chosen angular speeds from a randomly selected position on a spiral path and perform a three-way handshake to discover each other on an LOS link. The nodes change their angular speeds if the discovery is not successful within an optimal time interval, which is set by performing a number of test runs by placing each node at random positions. We evaluate the performance of the proposed approach through real test-bed experiments. The results show that, using such mechanically steerable highly directional transceivers, two neighbor nodes can discover each other successfully even without prior location information of each other. Key insights and contributions of this work include:

- An in-band method for two nodes in 3D to discover each other without prior knowledge of

[1]This work was published in ACM CoNEXT Workshop 2019[85].

the neighbor's location using only highly directional transceiver.

- A heuristic protocol that chooses an angular speed randomly, and updates the speed after threshold times.
- We observed from the experiments that neighbor discovery is possible using in-band full-duplex directional transceivers.

(a) (b)

Figure 4.1: (a) Mounted IBFD-FSO transceiver on DJI M100 Quad Drone, (b) Experimental setup for asynchronous spiral LOS discovery experiments.

4.1 Asynchronous Spiral Scanning

We explored asynchronous spiral neighbor discovery algorithm to establish a LOS link between two aerial vehicles. The nodes are positioned randomly in 3D space and each node carries an IBFD FSO transceiver mounted on servo motors. The transceiver is designed using two commercially available IrDA2 units to ensure full-duplex configuration [77, 86]. No additional omni-directional RF channel is used for synchronization or data transmission. The neighbor discovery method is to scan the surrounding 3D space by rotating the transceivers in randomly chosen spiral paths in 3D [86, 8]. Each node arbitrarily chooses an angular speed (ω) and a start position ($P(\phi,\theta)$) on the predefined spiral path to start the discovery process. LOS discovery is completed when they

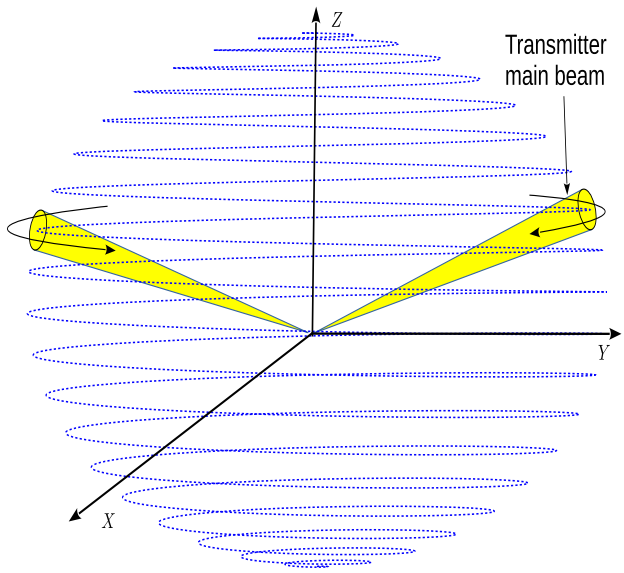

Figure 4.2: Spiral search space for the transceiver.

are able to perform a 3-way handshake between the two nodes. Figure 4.1(a) shows the path of the transceiver head for spiral scanning. For asynchronous discovery, initial start point ($P(\phi, \theta)$) is also randomly set, where ϕ and θ are angles w.r.t. z-axis and x-axis, respectively.

One of the corner cases of asynchronous LOS discovery is the case when angular speeds (ω) of the two nodes are same or very similar, which may result in longer discovery time [87]. By choosing random initial start point, we can increase the probability of discovery. But it is also important to reassign a new value to ω after a certain reset time (t_{reset}), since the benefit of randomly searching for the other node diminishes quickly. The algorithm for the LOS discovery phase using asynchronous spiral scan is given in Algorithm 2.

For these experiments, the angular speed, ω, is chosen by a node randomly, where $\omega \in [\pi/2, \pi]$ rad/s. The range of available ω is limited by the capabilities of the servo motors. For our prototype, the servo motors have maximum angular speed of π rad/s. To determine the reset time, t_{reset}, we conducted multiple LOS discovery runs and chose t_{reset} for a given confidence level (α) from the

Algorithm 2 Asynchronous Spiral LOS Discovery

```
Input Parameter t_reset // Reset time
R_x = TRUE // Start reception?
T_x = TRUE // Start transmission?
while T_x = TRUE do
    set ω randomly // Transceiver head angular speed
    set P(φ, θ) randomly // Transceiver head position
    start rotation in spiral path
    t = timer.start() // Discovery time
    while t < t_reset or R_x = TRUE do
        transmit 'HELLO'
        if 3-way handshake protocol completed then
            t = timer()
            stop transceiver head rotation
            R_x = FALSE
            T_x = FALSE
            write t to datafile
        end if
    end while
end while
```

empirical distribution.

Figure 4.3 shows the distribution and CDF of the LOS discovery time, repeated for 111 times, while the drone was hovering. From the experimental data, we can see that average discovery time is 62.68 sec and discovery is completed within 144.76 sec 90% of the time, whereas it is completed within 38.34 sec 50% of the time. It should be noted here, the reset time can be different for different confidence level (α) and divergence angle (β). We have listed the calculated reset times for different α from the empirical distribution in Table 4.1. The average discovery time for a two-node system can be further improved by optimizing t_{reset}, ω, and α.

Table 4.1: Reset time for different confidence level

α	0.1	0.3	0.5	0.7	0.9
t_{reset} (sec)	6.31	19.56	38.39	74.26	144.76

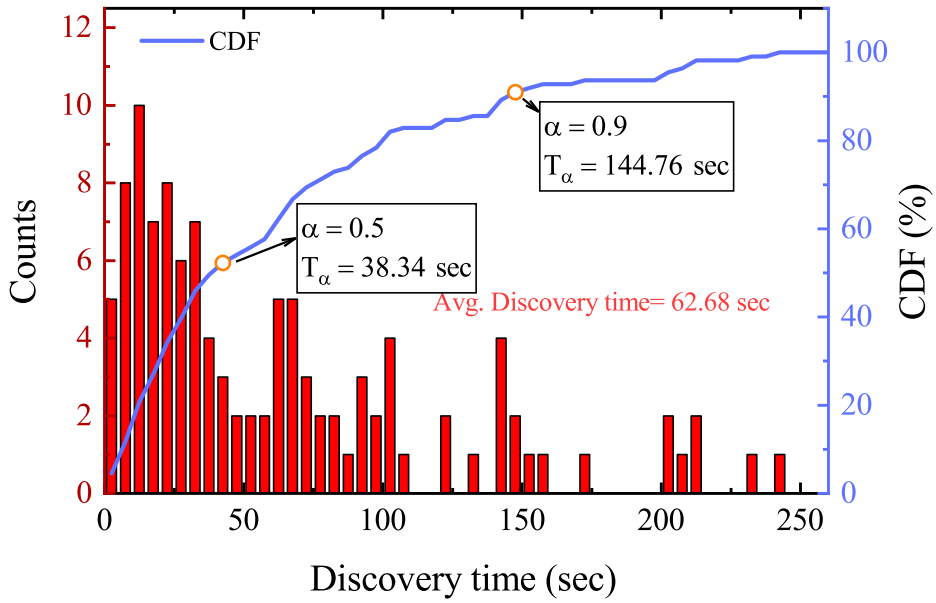

Figure 4.3: Empirical discovery time distribution.

4.2 Asynchronous Random Circular Scanning

We also explored asynchronous random circle scanning method to establish LOS between two mobile nodes. Similar to the previous approach, the nodes are positioned randomly in 3D space and each node carries an IBFD FSO transceiver mounted on servo motors. The neighbor discovery method is to scan the surrounding 3D space by rotating the transceivers in randomly generated circular paths in 3D. The Transceiver rotates three (3) times on a specific circle and then hops to another random circle. The transceiver keeps hopping to random circles until it can discover the other transceiver and establish LOS. The scanning space generated by the random process is shown in Fig. 4.4. The initial start point ($P(\phi, \theta)$) is also randomly set, where ϕ and θ are angles w.r.t. z-axis and x-axis, respectively.

The angular speed (ω) is chosen randomly, similar to the asynchronous spiral scanning approach.

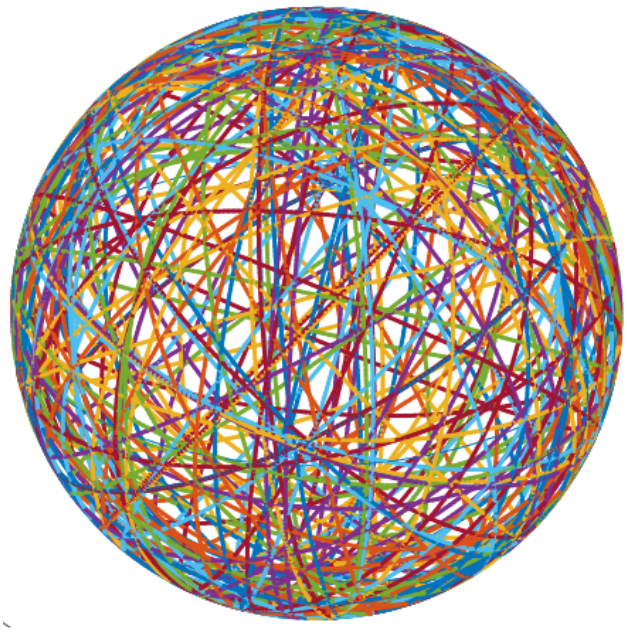

Figure 4.4: Random circles to generate search space for the transceiver.

However, the angular speed randomization for this approach has significantly smaller impact on discovery time compared to spiral scanning approach. We tested the random circle approach to establish LOS using real test-bed experimentation. We used the same system as described in Section 4.1. The LOS discovery completes when the nodes complete a three-way handshake protocol. We verified the algorithm by running the discovery process in the indoor settings with nodes at stationary conditions. We repeated the discovery process for 25 times in the outdoor setting with mobile nodes. The distribution function of the discovery algorithm for mobile nodes is shown in Fig. 4.5.

Comparing the indoor and outdoor distribution of the discovery time, we have found that average discovery time are 90.72 sec and 77.46 sec for indoor and outdoor settings, respectively. The distribution follows the log-normal distribution and 95% confidence interval time is 30.37 sec for outdoor settings. Comparing the average discovery time to the spiral scan, random circle approach

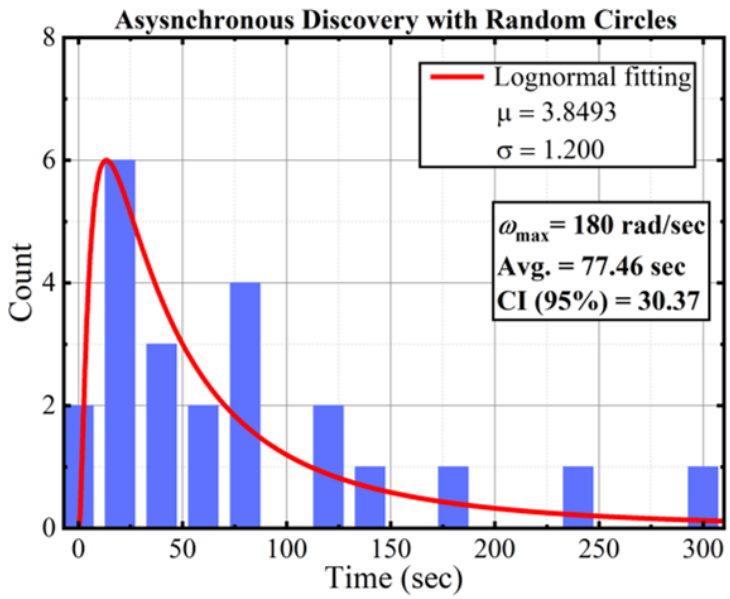

Figure 4.5: Empirical discovery time distribution for random circles.

takes longer time, which is expected as the advantage of random process diminishes as times passes.

In summary, we present an asynchronous LOS discovery algorithm using spiral scanning without any synchronization via an RF channel. Line-of-Sight (LOS) link discovery is one of the major limiting factors for these highly directional bands, and this problem of establishing LOS between neighbor nodes becomes more challenging when they have no apriori knowledge of the location of each other. We presented a demonstration of LOS discovery algorithm utilizing our developed in-band full-duplex FSO transceiver prototype in real-world application. We have presented multiple neighbor discovery algorithms in 3-D domain which establish LOS communication link between two mobile nodes. We also demonstrate the effectiveness of the algorithm through test-bed experiments using a prototype of UAVs equipped with in-band full-duplex (IBFD) FSO transceivers.

CHAPTER 5: MULTI-ELEMENT FSO TRANSCEIVER DESIGN USING OPTIMUM TILING

In this chapter, we will address the design and tiling of different elements, i.e., transmitters and receivers, on the transceiver plane to optimize IBFD communication throughput. We explore optimization techniques to find the optimum number of transmitters and tiling those in a fashion that gives uninterrupted performance even in the presence of vibration. The main contributions are as follows:

- An analytical model of link performance parameter, SINR, is developed for multi-element full-duplex FSO transceiver by considering free-space attenuation as well as the vibration model of the mobile platform, e.g., an unmanned aerial vehicle (UAV).
- An optimized approach of tiling elements within transceiver plane by evaluating randomly generated sets.
- An optimized approach of tiling elements within transceiver plane by implementing genetic algorithm and evaluating multiple generations of solutions to reach the most favorable tiling pattern.

5.1 Optical Channel Fading Model

5.1.1 Channel Model

The transmitter modulates data onto the instantaneous intensity of an optical beam. In this chapter, we consider intensity modulated direct detection channels using On-Off Keying (OOK), which is

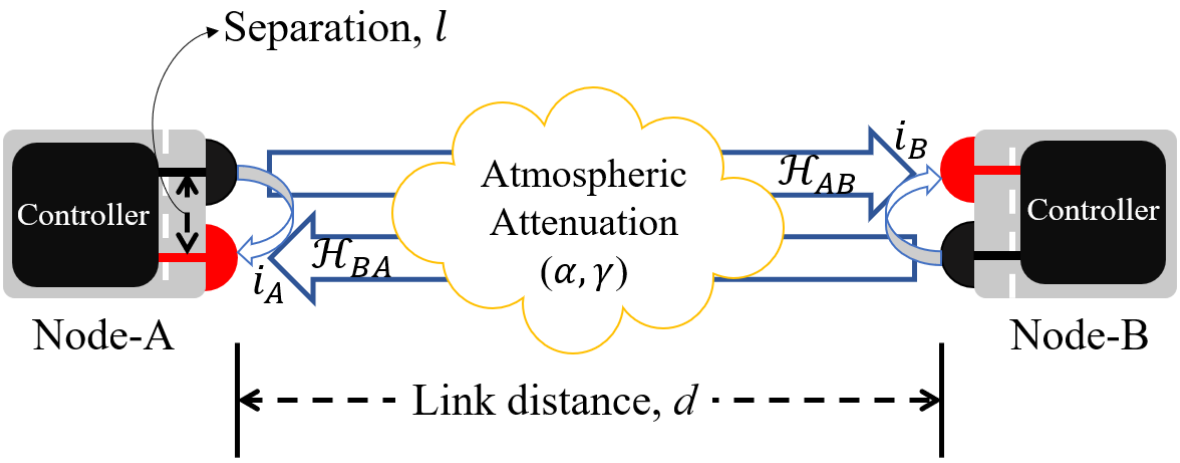

Figure 5.1: Block diagram of an in-band full-duplex optical wireless link consisting of two nodes.

widely employed in practical systems. The received photocurrent signal is related to the incident optical power by the detector responsivity R. The received signal y suffers from a fluctuation in signal intensity due to atmospheric turbulence and misalignment, as well as additive noise, and can be well modeled as

$$y = hRx + n + i_S, \tag{5.1}$$

where x is the transmitted signal intensity, h is the channel state, i_S is the SI signal received at the receiver from its own transmitter, y is the resulting electrical signal, and n is signal-independent additive white Gaussian noise. The system block diagram consists of two nodes, A and B, as presented in Fig. 5.1. It also shows the signal flow direction at the presence of atmospheric attenuation parameters (α, γ), which will be discussed in details later.

The channel state h models the random attenuation of the propagation channel. In our model, h arises due to three factors: path loss h_l, geometric spread and pointing errors h_p, and atmospheric turbulence h_a. The channel state can then be formulated as

$$h = h_l h_p h_a. \tag{5.2}$$

Note that h_l is deterministic, and h_p and h_a are random with distributions discussed later. Since the time scales of these fading processes ($\approx 10^{-3} - 10^{-2}$ s) are far larger than the bit interval ($\approx 10^{-9}$ s), h is considered to be constant over a large number of transmitted bits. Notice that the use of interleaving to allow for averaging over a large number of fading states is impractical in this channel. This block fading channel is often termed as slow fading or nonergodic channel in which an h is chosen from the random ensemble according to distribution $f_h(h)$ and fixed over a long block of bits.

5.1.2 Optical Fading Model

Optical fading can be attributed to several components of the channel and communication system design. Three major components of optical fading in the channel are atmospheric turbulence, free-space attenuation, and pointing error due to misalignment.

5.1.2.1 Free-Space Attenuation

The attenuation of laser power through the atmosphere is described by the exponential Beers-Lambert Law as [68]

$$h_l(z) = \frac{P(z)}{P(0)} = \exp(-\alpha z), \tag{5.3}$$

where $h_l(z)$ is the loss over a propagation path of length z, $P(z)$ is the laser power at distance z, and σ is the attenuation coefficient. The attenuation h_l is considered as a fixed scaling factor during a long period of time, and no randomness exists in its behavior. It depends on the size and distribution of the scattering particles and the wavelength utilized. It can be expressed in terms of the visibility, which can be measured directly from the atmosphere.

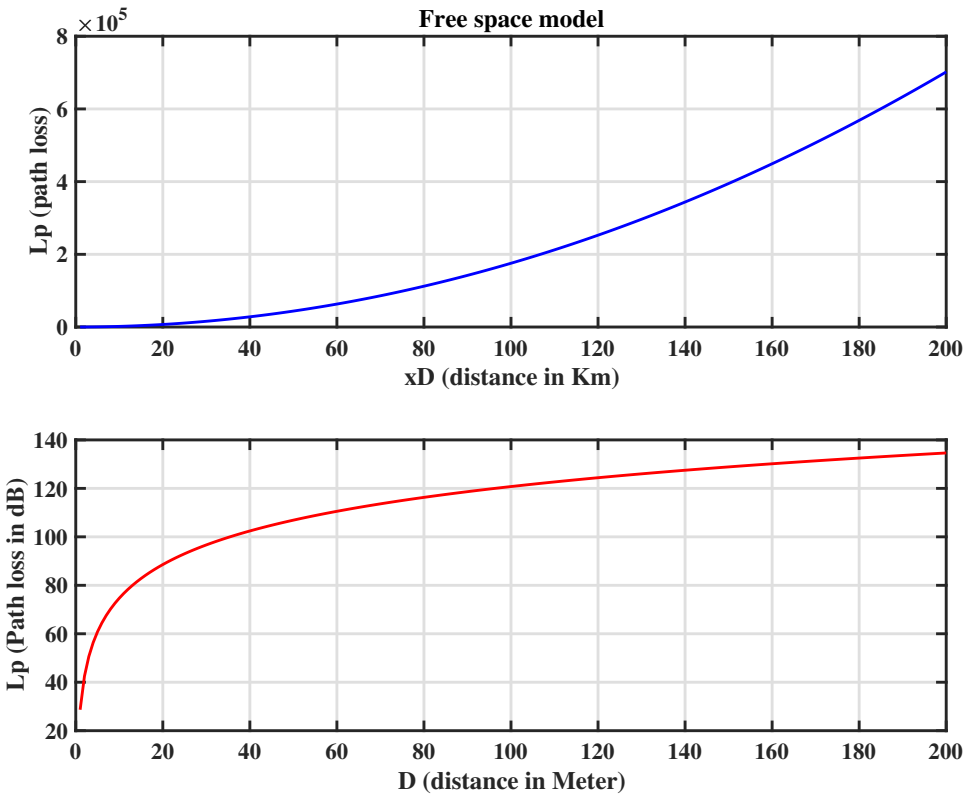

Figure 5.2: Path loss calculation for free-space fading model.

By using Friis transmission equation [66], we can calculate the attenuation coefficient as

$$\alpha = \frac{1}{d} \ln \frac{1}{G_T G_R T_A L_{FS}}. \tag{5.4}$$

The value of α depends on wavelength of the signal λ, visibility range V, and size distribution of the particle q in the atmosphere. The equation of atmospheric attenuation coefficient is proposed by Kim *et al.* [69] in the form of

$$\alpha = \frac{3.91}{V} \left(\frac{\lambda}{550 \text{ nm}} \right)^{-q}, \tag{5.5}$$

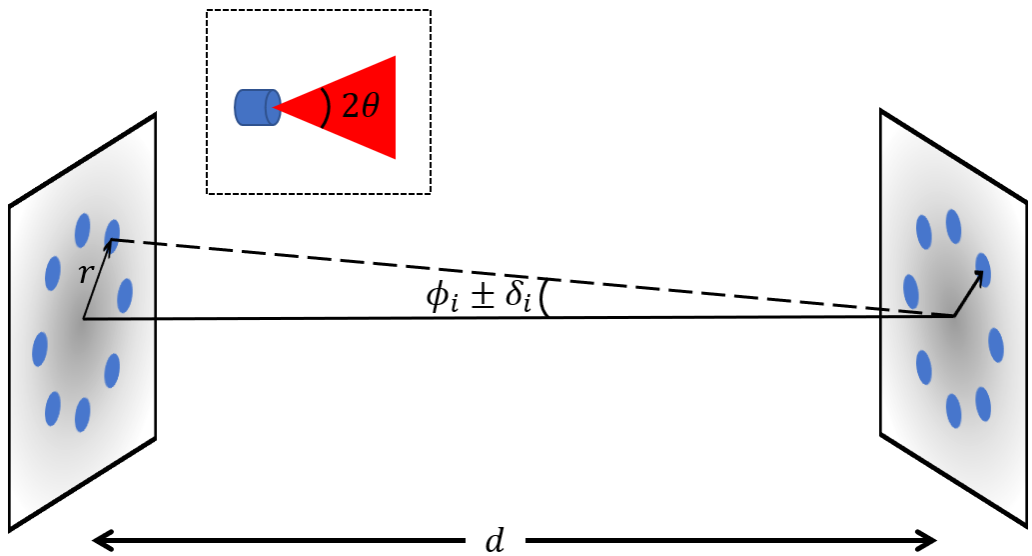

Figure 5.3: Orientation of the two communicating nodes after alignment.

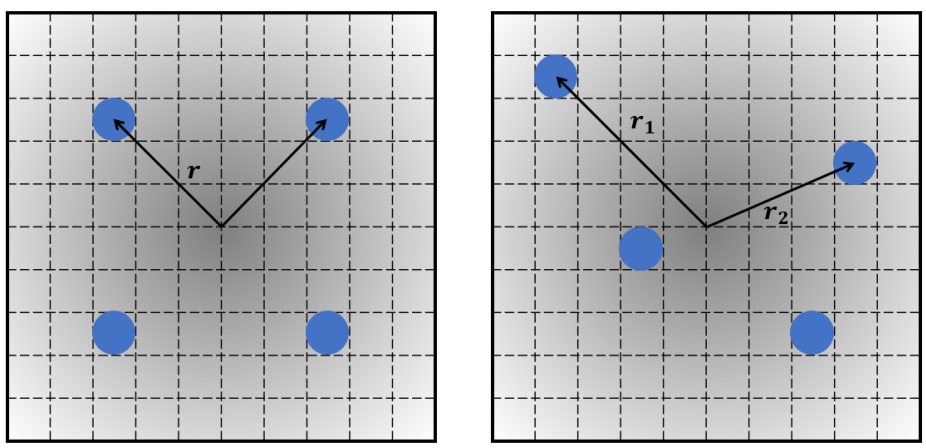

Figure 5.4: Position of transmitters within a transceiver plane.

where q is given by

$$q = \begin{cases} 1.6; & V > 50 \text{ km} \\ 1.3; & 6 \text{ km} < V < 50 \text{ km} \\ 0.72V^{\frac{1}{3}}; & V < 6 \text{ km}. \end{cases} \tag{5.6}$$

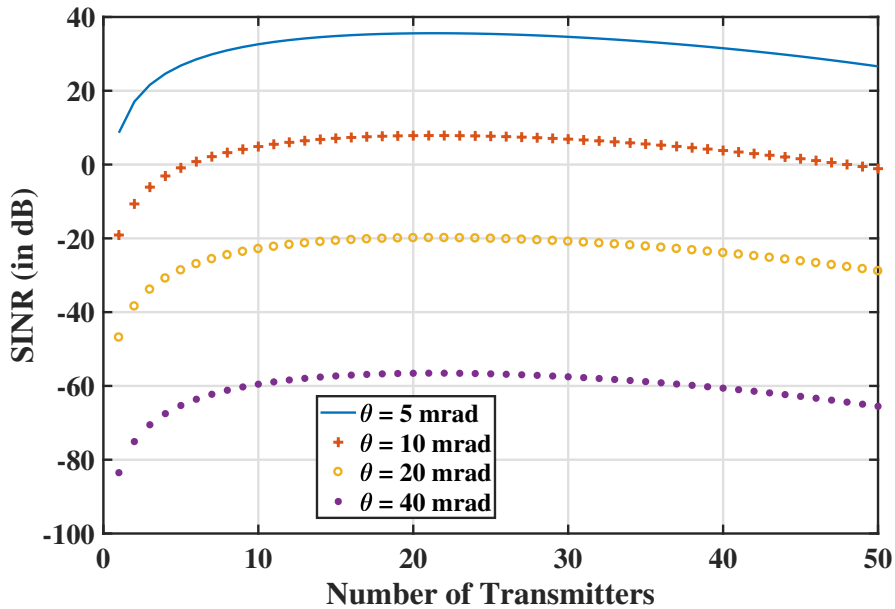

Figure 5.5: SINR calculation for different divergence angles of the transmitters, while $d = 100$ m, $\phi = 3.4$ mrad, and $P_T = 10$ mW.

Using the equations 5.4-5.6, we have calculated the free-space path loss components with respect to the link distance (d). The loss parameter model (L_p) is shown in Fig. 5.2.

5.1.2.2 Pointing Error

Loss of LOS or LOS alignment could result in significant channel fading due to pointing error loss. Wind, gust, and thermal expansion of atmospheric medium results in path delay and/or pointing error. We discuss a statistical model to incorporate such pointing error in term of detector aperture, Gaussian beam width, and jitter and vibration variance.

The normalized spatial intensity distribution of the transmitted Gaussian beam is given by [88]

$$I_{beam}(\rho;z) = \frac{2}{\pi w_z^2} \exp\left(-\frac{2||\rho||^2}{w_z^2}\right), \tag{5.7}$$

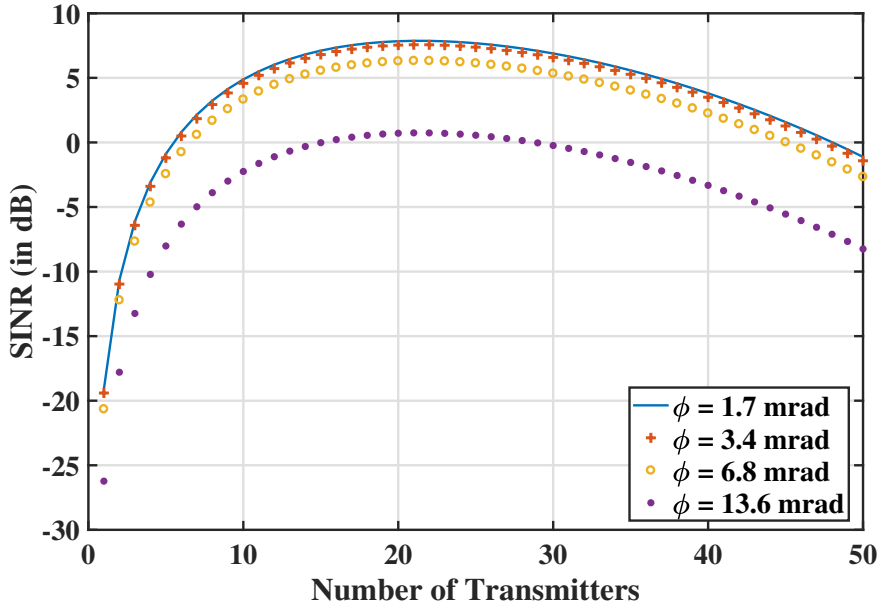

Figure 5.6: SINR calculation different positioning of transmitters in the transceiver plane, while $d = 100$ m, $\theta = 10$ mrad, and $P_T = 10$ mW.

where ρ is the radial vector from the beam center and w_z is the Gaussian beam waist at distance z, which can be written as

$$w_z \approx w_0 \left[1 + \varepsilon \left(\frac{\lambda z}{\pi w_0^2} \right)^2 \right]^{1/2}, \tag{5.8}$$

where, w_0 is the beam waist at $z = 0$, $\varepsilon = (1 + 2w_0^2/\rho_0^2(z))$, and coherent length, $\rho_0(z) = (0.55 C_n^2 k^2 z)^{-3/5}$.

If the center of the incident beam is misaligned by distance r along detector plane, then the fraction of the power collected by the detector, $h_p(.)$, can be expressed as

$$h_p(r;z) = \int_{\mathscr{A}} I_{beam}(\rho - r; z) d\rho, \tag{5.9}$$

where $\mathscr{A}$ is the area of the detector and h_p is a function of radial misalignment angle when pointing error r is present, as shown in Fig. 5.3 and 5.4. Due to symmetry in beam shape and detector area,

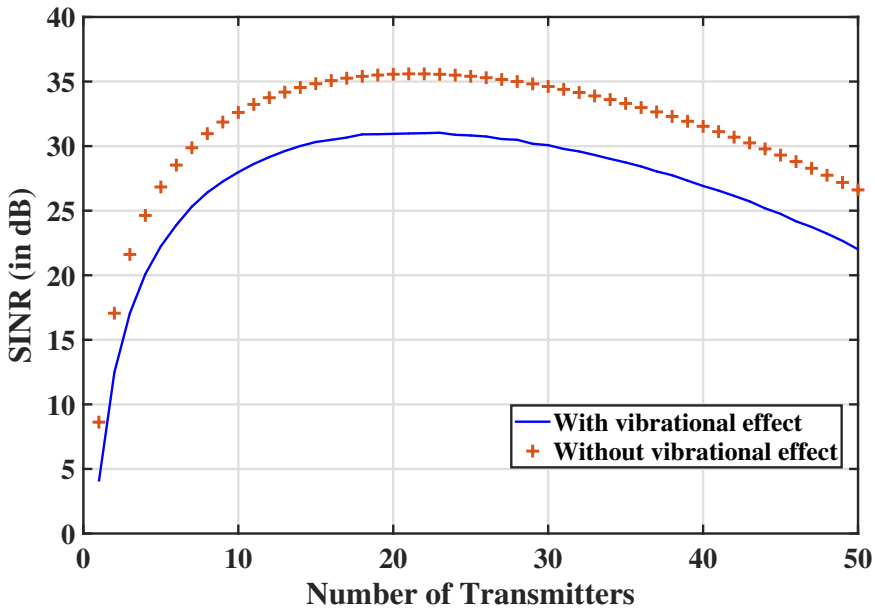

Figure 5.7: Effect on SINR at the presence of vibration of the mobile platform for $d = 100$ m, $\phi = 1.7$ mrad, $\theta = 5$ mrad, and $P_T = 10$ mW.

the integral can be approximated by

$$h_p(r;z) \approx A_0 \exp\left(-\frac{2r^2}{w_{z_{eq}}^2}\right), \tag{5.10}$$

where

$$A_0 = [\mathrm{erf}(v)]^2$$

$$w_{z_{eq}}^2 = w_z^2 \frac{\sqrt{\pi}\mathrm{erf}(v)}{2v\exp(-v^2)}$$

$$v = \frac{\sqrt{\pi}a}{\sqrt{2}w_z},$$

and a is the radius of a single receiver.

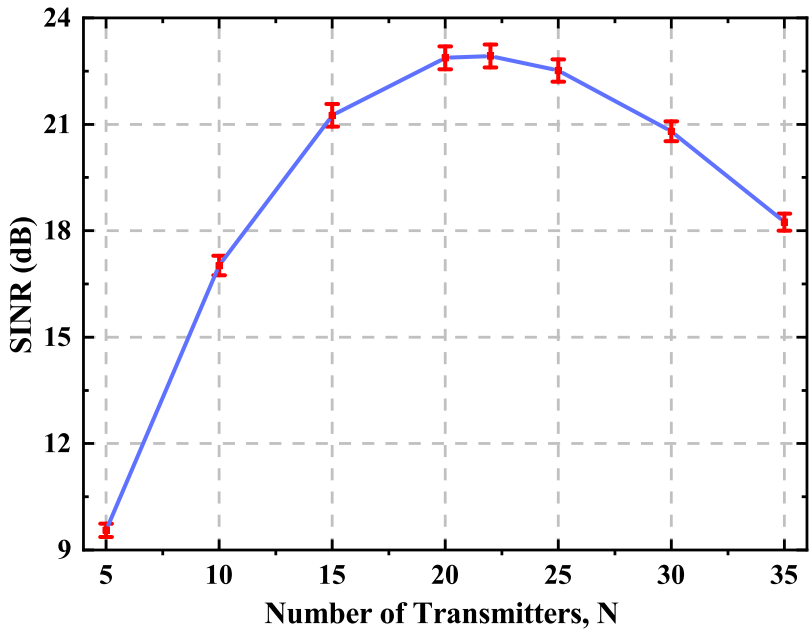

Figure 5.8: Variation of SINR when transmitters with $\theta = 5$ mrad divergence angle are placed randomly on 10×10 transceiver grid, while $d = 50$ m and $P_T = 10$ mW.

5.2 IBFD FSOC Link: SINR Formulation

5.2.1 Noise and Self-Interference

The noise components when an optical signal is received by the detector consist of various noise sources like Johnson (thermal) noise, background radiation, and dark current. The equations for the noise equivalent power (NEP) of the optical components are given by [74]

$$P_{bg\_sn} = \frac{\sqrt{2qSP_{bg}B_{en}F}}{S}, \tag{5.11}$$

$$P_{sig\_sn} = \frac{\sqrt{2qSP_{sig}B_{en}F}}{S}, \tag{5.12}$$

$$P_{dark\_sn} = \frac{\sqrt{\left(2qI_{dark}G_{det}^2F + 2qI_{dc}\right)B_{en}}}{SG_{det}}, \tag{5.13}$$

where P_{bg} is the optical solar background noise, P_{sig} is the optical power of the signal, I_{dark} is optical dark current, I_{dc} is the DC dark current, G_{det} is the detector current gain, B_{en} is effective noise bandwidth ($= \frac{\pi B}{2}$), S is radiant sensitivity of the detector (amp/watt), F is excess noise factor which is equal to 1 for photodiode, and q is the electronic charge. The total NEP is given by

$$N_T = \sqrt{P_{bg\_sn}^2 + P_{sig\_sn}^2 + P_{dark\_sn}^2}. \tag{5.14}$$

To design a short-range FSOC system using laser as transmitter, all the noise contributions need to be incorporated in calculation. As the bit-rate requirement is increasing day-by-day, receiver components and circuit are required to be very sensitive and responsive. With the increase of sensitivity, receiver noise budget is becoming smaller.

By using the residual SI model of [75, 63], residual SI power at nodes A and B are given by $\Gamma_{sA} = \frac{P_A^{1-\delta}}{\beta\mu^{\delta}}$ and $\Gamma_{sB} = \frac{P_B^{1-\delta}}{\beta\mu^{\delta}}$, where β represents the coefficient of SI suppression by separation of the transmitter and the receiver within the same transceiver unit, and μ and δ represent SI suppression parameters for deployed passive SI cancellation technique. P_A and P_B are the transmitted signal power at nodes A and B, respectively.

5.2.2 Optimized SINR Formulation

SINR characterizes the quality of a communication system as well as it is the performance parameter for a transceiver. Considering an FSO link established using transceivers A and B, each with a single transmitter having a divergence angle of θ and a single receiver having a detection area of

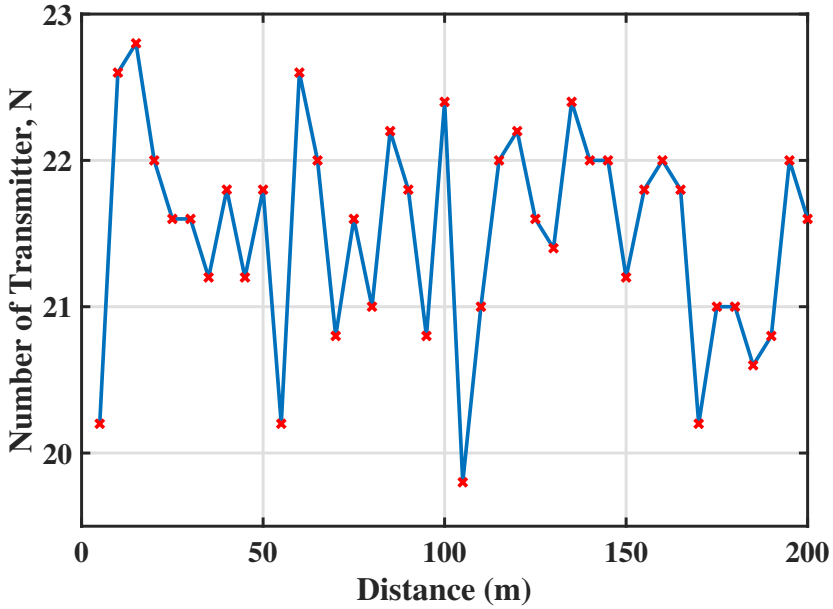

(a)

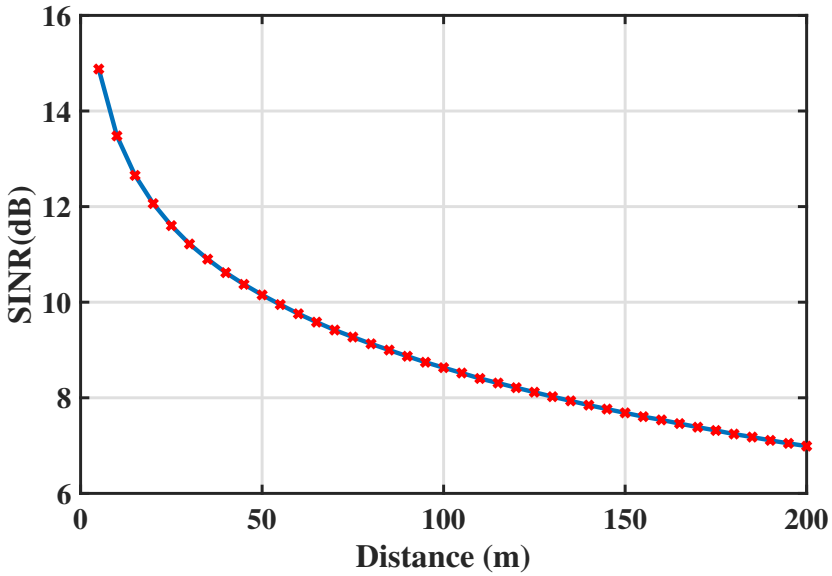

(b)

Figure 5.9: (a) Optimum number of transmitter (N) and (b) SINR variation for different link range (d).

A_{det}, SINR can be written for node A as [74]

$$SINR_A = \left[\frac{P_B L_z(d,\lambda) A_{det} \cos(\phi \pm \delta)}{(\tan\theta)^2 4d^2 (N_T + \Gamma_{SA})}\right]^2, \tag{5.15}$$

where P_B is the transmit power at node B, d is the link distance, and $L_z(d,\lambda)$ is the free-space loss parameter for a link distance of d. The expressions of L_z, N_T, and Γ_{SA} are shown in Sections 5.1 and 5.2.1. ϕ is the pointing error angle when the transceivers are perfectly aligned, and δ is the 'vibration angle' which is the additional pointing error due to vibration on the mobile transceivers.

For a multi-element FSO transceiver with N transmitters having θ divergence angle each and m receivers with detection area of A_{det}, SINR for node A can be expressed as

$$SINR_A = \sum_{i=1}^{N} \sum_{j:j\in\mathscr{F}_i} \left[\frac{P_{B,i} L_z(d,\lambda) A_{det} \cos(\phi_j \pm \delta_j)}{(\tan\theta)^2 4d^2 (N_T + \Gamma_{SA})}\right]^2, \tag{5.16}$$

where i and j denote the index of transmitter and receiver, respectively. $P_{B,i}$ denotes the transmit power at transmitter i at node B. Each transmit beam projects a beam footprint on the transceiver plane and only covers a subset of the available receivers in a transceiver. $\mathscr{F}_i$ represents the set of receivers that falls within the beam footprint of transmitter i. ϕ_j and δ_j are the pointing error and the vibration angles on the beam arriving at receiver $j \in \mathscr{F}_i$.

To maximize SINR, we need to find the optimum number of transmitters N and receivers m, as well as the positions, $p_i(x_i, y_i)$, of the transmitters onthe transceiver plane. By choosing the best transmitter positions we can find the best tiling patterns of the transceivers. For the sake of uniformity, we will consider identical tiling at both transceiver nodes A and B, same divergence angle θ for all transmitters, and same transmit power P_B for all transmitters. So, the optimization problem

becomes

$$\begin{aligned} \max_{N,\ p_i} \quad & SINR_A \\ \text{s.t.} \quad & N < N_m, \\ & A_T = NA_{trans} + mA_{det}, \end{aligned} \tag{5.17}$$

where A_{trans} is the area of each transmitter occupied in the transceiver plane and N_m is the maximum number of transmitters that can be placed on the transceiver plane. We do not include m as a parameter of the optimization since we assume that for all the positions where a transmitter is not placed, a receiver is placed, i.e., $N_m = N + m$.

Each transmitter i projects a Gaussian beam footprint on the receiver plane centered at the corresponding location of transmitter i with a diameter of $d \tan\theta$. $\mathscr{F}_i$ consists of m_i' receivers that falls within the beam footprint. So, the SINR of the IBFD FSO link at node B under no vibration can be written as

$$SINR_A = \sum_{i=1}^{N} \Pi_i, \tag{5.18}$$

where

$$\Pi_i = \sum_{j:j\in\mathscr{F}_i} \left[\frac{P_B L_z(d,\lambda) A_{det} \cos(\phi_j)}{(\tan\theta)^2 4d^2 (N_T + \Gamma_{SA})} \right]^2. \tag{5.19}$$

We find the optimum transmitter count, N^*, maximizing $SINR_A$ by calculating $\frac{\partial}{\partial N}(SINR_A) = 0$. Using Eq. 5.18 we get

$$\begin{aligned} \frac{\partial}{\partial N}(SINR_A) &= \frac{\partial}{\partial N} \sum_{i=1}^{N} \Pi_i \\ &= \frac{\partial}{\partial N}(\Pi_1 + \Pi_2 + ... + \Pi_N). \end{aligned} \tag{5.20}$$

Each term of Π_i on the right hand side of Eq. 5.20 largely depends on the relative location of the transmitter i, as that determines how many receivers (m_i') are covered by the beam footprint.

Increase of transmitters also means reduction of receivers, essentially resulting in reduced receiver area to capture the beam signal. So, the ratio of the total receiver area to the total transceiver area is another parameter that can be used to optimize *SINR*. In order to attain an analytical solution to N^*, we consider the case when this ratio is fixed, i.e., m_i' is constant regardless of i. This case happens when the link distance (d) is long and/or the divergence angle (θ) of the transmitters is large. In particular, this case would happen when the radius of the beam footprint is greater than or equal to the diagonal of the transceiver plane. Assuming that both transmitters and receivers are square-shaped and are the same in size (i.e., the receiver and the transmitter areas are both equal to A_{det}), this case would happen when $d\tan\theta \geq \sqrt{2N_m A_{det}}$. Then, $\mathscr{F}_i$ consists of all the available receivers on the transceiver which yields $m_i' = N_m - N$, and Eq. 5.19 becomes

$$\Pi_i = \sum_{j=1}^{N_m - N} \chi_i \left(1 - \frac{\phi_j^2}{2}\right)^2, \tag{5.21}$$

where $\chi_i = \left[\frac{P_B L_z(d,\lambda) A_{det}}{(\tan\theta)^2 4 d^2 (N_T + \Gamma_{SA})}\right]^2$, and $\cos(\phi_j)$ is approximated with the first two terms of Taylor expansion. Now, each receiver has pointing error angle with respect to each transmitter. If the transmitters and receivers are uniformly distributed, the pointing error angle can be approximated by $\phi_j = j\phi$, where ϕ is the minimum pointing error angle. Then, Eq. 5.21 can be written as

$$\Pi_i = \chi_i \Big[(N_m - N) - \phi^2 \frac{(N_m - N)(N_m - N + 1)(2N_m - 2N + 1)}{6}\Big]. \tag{5.22}$$

As we assumed every transmitter's beam footprint is covering the whole transceiver area, each Π_i

becomes identical. By using the expression from Eq. 5.22, Eq. 5.18 can be written as

$$\begin{aligned} SINR_A = \chi N \Big[& (N_m - N) - \frac{\phi^2}{3} N_m^3 + \phi^2 N_m^2 N \\ & - \phi^2 N_m N^2 + \frac{\phi^2}{3} N^3 - \frac{\phi^2}{2} N_m^2 + \phi^2 N_m N \\ & - \frac{\phi^2}{2} N^2 - \frac{\phi^2}{6} N_m - \frac{\phi^2}{6} N \Big]. \end{aligned} \tag{5.23}$$

By differentiating the term from Eq. 5.23, we get

$$\begin{aligned} \frac{\partial}{\partial N}(SINR_A) = \chi \Big[& N_m - 4N + 2\phi^2 N_m^2 N - 3\phi^2 N_m N^2 \\ & + \frac{4}{3}\phi^2 N^3 + 2\phi^2 N_m N - 3\frac{\phi^2}{2} N^2 - \frac{\phi^2}{3} N \\ & - \frac{\phi^2}{3} N_m^3 - \frac{\phi^2}{2} N_m^2 - \frac{\phi^2}{6} N_m \Big]. \end{aligned} \tag{5.24}$$

By simplifying the equation and setting $\frac{\partial}{\partial N}(SINR_A) = 0$, we get

$$aN^3 + bN^2 + cN + d = 0, \tag{5.25}$$

where

$$\begin{aligned} a &= \frac{4}{3}\phi^2, \\ b &= -\frac{\phi^2}{2} - 3\phi^2 N_m, \\ c &= 2\phi^2 N_m^2 + 2\phi^2 N_m - 4 - \frac{\phi^2}{3}, \\ d &= N_m - \frac{\phi^2}{6} N_m - \frac{\phi^2}{2} N_m^2 - \frac{\phi^2}{3} N_m^3. \end{aligned}$$

Now, the value of N_m can range from few tens to few hundreds and ϕ is in the order of mrad for

practical cases. In that case, the coefficients approximated as $a \approx 0$, $b \approx 0$, $c \approx -4$, and $d \approx N_m$. The optimum number of transmitter reduces to $\frac{N}{N_m} \approx 0.25$. This solution represents the case when pointing error angles are negligible. However for practical cases, due to finite pointing error angles the optimum solution for N^* is smaller than $0.25N_m$.

In the following section, we implemented a numerical solution of the optimization problem by using randomly generated sets. First we calculated the optimum number of transmitters (N) and then the optimum positions (p_i) of the transmitters on the transceiver plane. We also implemented a genetic evolution algorithm technique to find the optimum positions of the transmitters.

5.3 Approach One: Randomly Generated Sets

To determine the optimum tiling positions of the transceiver elements, we developed a MATLAB tool to simulate the communication link and calculate *SINR* for each node. For this simulation, we used 50 m long FSO channel between two UAVs communicating in IBFD mode using wavelength λ = 900 nm. The transceiver size is set to 10 cm $\times$ 10 cm. We assume that direct LOS is already established, however the vibrational effects from the UAVs is still present which can lead to pointing error of the link.

As the position of each transmitter is varied on the transceiver plane, a pointing error with the other node takes place. This pointing error is calculated in terms of pointing angle, ϕ. On top of this angular pointing error ϕ, vibration of the mobile platform incorporates additional error, which is also calculated in terms of angular error ($\pm\delta$). These pointing angle errors are shown in Fig. 5.3. Figure 5.4 shows two categories of possible tiling schemes. In one scheme, all the transmitters are positioned equidistant from the center of the transceiver plane. On the other hand, all transmitters are positioned randomly in the second scheme. In this case, we randomly selected

N transmitter slots and the rest are considered to be receiver area. Free-space path loss is calculated for determining *SINR* for our channel, which is shown in Fig. 5.2.

To determine the number of the transmitters required to obtain the best performance, we simulated the FSO link by varying the transmitter count from 1 to 99, out of possible 100 positions, and calculated *SINR* for different divergence angles (θ). We can observe from Fig. 5.5 that best performance of the link occurs when number of transmitters (N) is 22, irrespective of divergence angles. With the increase of the transmitter count, receiver area reduces and that results into degraded link performance. Also, by increasing divergence angle, most of the power collected at the receiver end also reduces, and we can observe the reduction of *SINR*.

We investigated further by varying the position of the transmitters on the transceiver plane and hence changing the pointing error angle (ϕ) by using equidistant scheme from Fig. 5.4. Fig. 5.6 shows the results for different ϕ values and calculated by varying N. We can again observe that the best case performance can be achieved for $N = 22$. Fig. 5.7 shows the effect of vibration on the link performance of the FSO channel. Fig. 5.8 shows the average and standard deviation of the calculated *SINR* for different N values. We also randomly generated vibrations and repeated the simulation for 1000 times to incorporate the effects of vibration into the simulation. Even though the overall *SINR* obtained is reduced by introducing vibration, best case scenario still occurs at $N = 22$, or we can say 22% area of the transceiver plane needs to covered with transmitters. Even when the link distance is varied over a large range, the optimum number of transmitters remains close to 22%, whereas average SINR drops exponentially with distance as shown in Fig. 5.9. By using the simulation parameters and solving the equation derived in Eq. 5.25, we get $N = 25$. The analytical solution was an approximation of the real-world scenario, however we got fairly close solutions.

We incorporated all the findings we gathered from the simulations of equidistant scheme into the

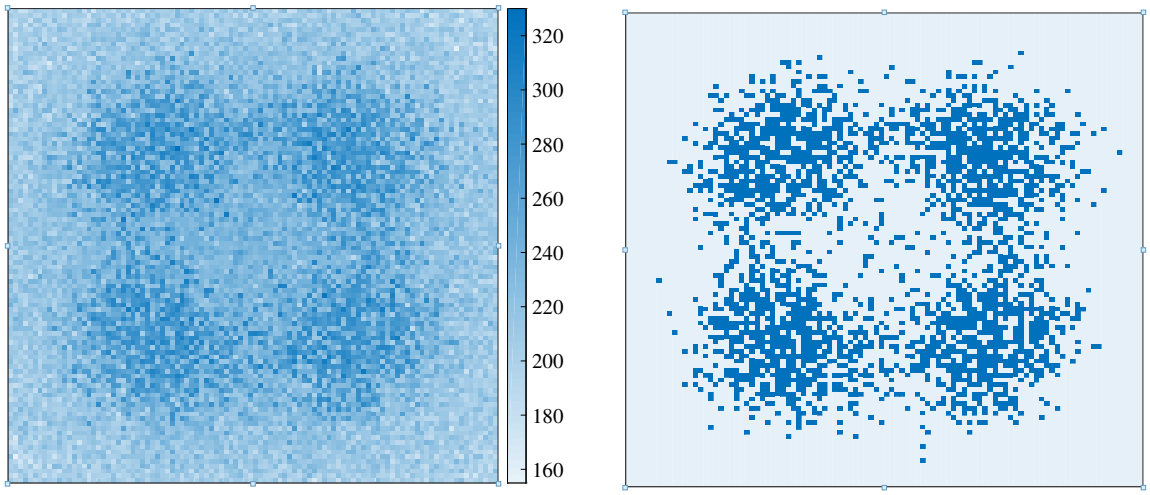

(a) (b)

Figure 5.10: (a) Heatmap of transmitter locations on a 100×100 transceiver grid for best performances out of randomly generated set, (b) Transmitter locations based on the heatmap generated from best performing sets.

random position scheme as shown in Fig. 5.4. We increased the grid size of the transceiver plane to 100×100 array. We generated $100,000$ sets of transceiver planes with randomly positioned transmitters for each N, in this case, to cover 22% area of the plane, we set $N = 2,200$. To determine the optimum positions of the transmitters for $N = 2,200$, we selected best $1,000$ sets out of randomly generated $100,000$ sets based on *SINR* performance. We repeated the process for 3 times with seed values. Finally, we constructed a heatmap of the transceiver plane by overlapping the best tiling sets (more dark means more transmitters were placed at that position in these tiling sets) in Fig. 5.10(a) at the presence of vibrational effects. We can observe from the figure that the best performance can be achieved when majority of the transmitters are positioned around the center of the plane, with receiving areas at the center. The reason for the disperse positioning due to the presence vibrational effects of the mounting platform is the Gaussian beam profile of the transmit signal and the beam centers carry most of the energy. If the transmitters are positioned

around the edges, the center of the beams might fall outside of the transceiver plane and most of the energy goes undetected at the presence of vibration. To accommodate for such cases, the optimum transmitter positions are clustered in four separate areas located midway from the center to the corners of the transceiver plane so that at least the center of the beams from those 'edge transmitters' could fall on the receiving plane.

It is notable that the center of the transceiver plane does include only few receivers instead of being entirely covered with transmitters. The intuition behind this is that the center of the optical beam carries most of the energy. If the center of the plane is covered entirely by transmitters, the center of the beams coming from the other plane would not be received and only the outer part of those beams would be received, resulting in a small aggregate received intensity. With the presence of vibration, however, the best transmitter positions are more dispersed to increase the likelihood of receiving the center of the beams coming from the other side.

This random set based technique of obtaining the optimum solution is computationally heavy and as we checked only a fraction of the available solutions due to limitation of computational capacity and time, hence a more efficient method is required. To overcome this computational complexity, we next devise a heuristic optimization method based on genetic algorithms.

5.4 Approach Two: Genetic Algorithm

In order to tackle the computational complexity of the randomized set selection and to find solutions closer to the optimum, we devise a genetic algorithm approach to the problem of tiling positions of the transmitters on the transceiver plane. As the transceiver plane is divided into a 100×100 grid, it gives us in total $10,000$ different position to consider for transmitters. Essentially the size of the search space for the optimization problem becomes $2^{10000} - 1$. Using the

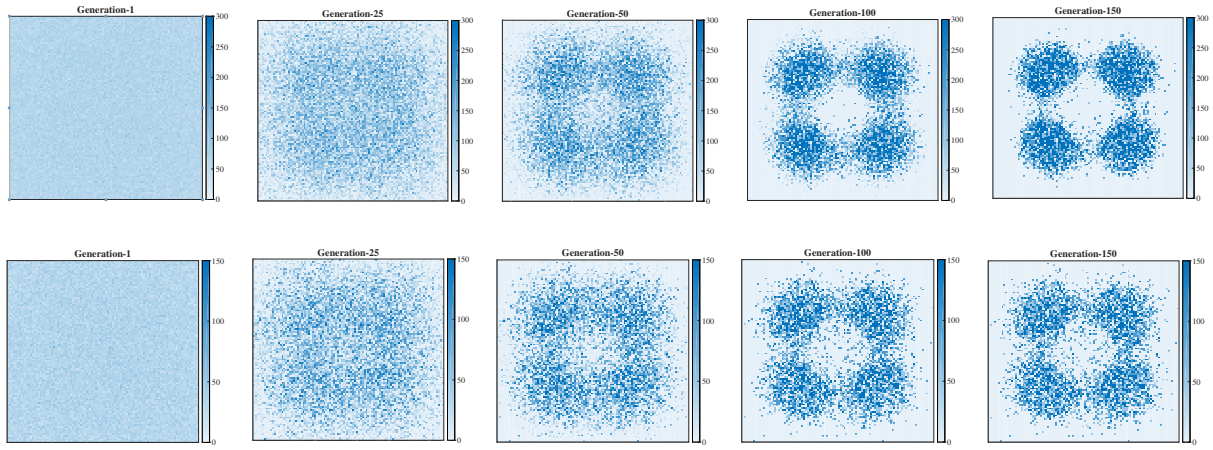

Figure 5.11: Heatmap of transmitter locations on a 100×100 transceiver grid for best performances for different generations of genetic evolution, Top Row: 20% fit population, Bottom Row: 10% fit population.

randomly generated sets to determine the optimum tiling will require huge computational time. Even in the optimization approach presented in the previous section, we only explored a fraction of the every possible tiling combination. Genetic algorithm gives a faster way to approach the optimum and it also requires smaller computational capacity.

To implement the genetic algorithm, we start with fewer number of randomly generated sets of the transceiver plane. To reduce the complexity of the problem, we consider 22% of the area is covered with transmitters, as we determined in the previous section. To start the process, we randomly generate $5,000$ different sets and calculate SINR for each set. We determine the best 10% sets out of the total population based on *SINR* calculation, which we can call the 'fit population'. We use the 'fit population' to generate the next generation by applying crossover technique. We randomly select two members from the current fit population to obtain a member of the next generation. The crossover is done over two steps: first, we identify the common positions of the two selected parents and we retain the common positions in the child. Second, we select rest of the transmitter positions from each parent in $1:1$ ratio. We repeat the process to obtain the entire population for

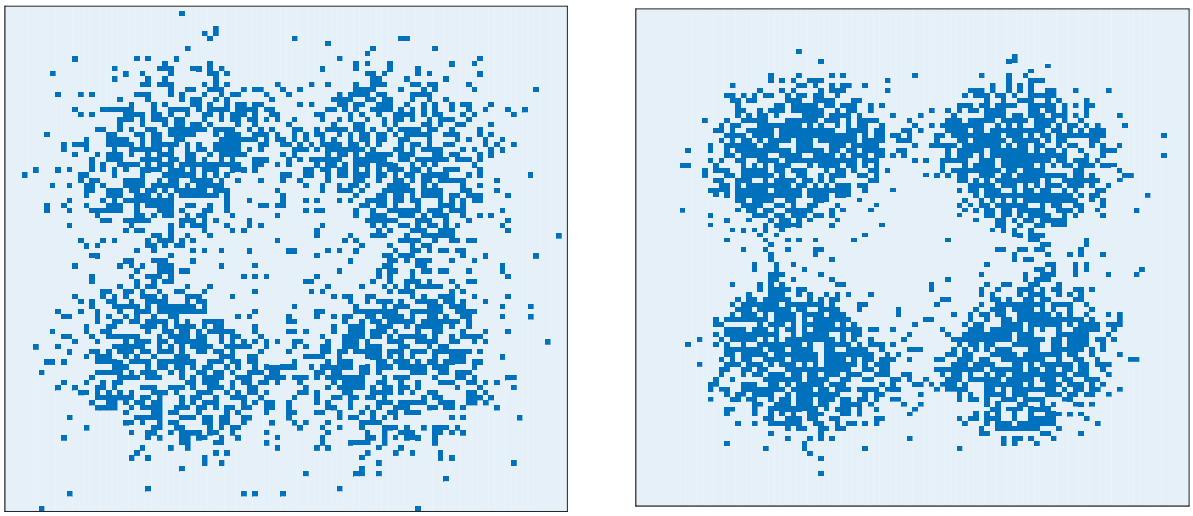

(a) (b)

Figure 5.12: Optimized transmitter locations on a 100×100 transceiver grid (a) using genetic evolution after generation 150 with 10% fit population with vibrational effect, (b) using genetic evolution after generation 150 with 20% fit population with vibrational effect.

the next generation and calculate SINR for each set. The process is repeated until we do not see any significant improvement in the average *SINR* value of the fit population for three (3) consecutive generations or a certain number of generations are obtained. A pseudo-code of the algorithm is presented in Algorithm 3.

We presented the evolution of the optimized tiling solutions over different generations in Fig. 5.11. The heatmaps are generated by overlapping the transmitter tiling positions of the members of the fit populations of each generation. We can observe from the figures that transmitters around the center with receiving area at the center gives best performance, as we observed from the randomly generated sets in the previous section. Hence, the convergence over the generations are observed as the transmitter locations are more clustered in four lobes located midway towards the corners of the transceiver plane from the center. We also changed the fit population size to 10% and observed the similar convergence pattern as well. After about 50 generations, both 20% and 10% fit population

Algorithm 3 Genetic Algorithm for Optimized Tiling

```
Initialize Transmitter count, N
Initialize Transceiver plane
Initialize Population Set count, P
Set ε as SINR tolerance
flag=TRUE
Generate Population Set by random selection for Generation 1
Calculate SINR for each set
while flag is TRUE do
    Identify Best f% as fit population seed for Generation i+1
    Generate Population Set by crossover() for Generation i+1
    Calculate SINR for each set
    Compare SINR with Generation i
    if SINR(i+1)−SINR(i)< ε for 3 consecutive generations then
        flag=FALSE
    else
        repeat next generation
    end if
end while
```

crossover()

```
Choose two (2) parents randomly from the fit population
Determine common transmitter positions for the parents
Keep common transmitter positions for the child
Choose rest of the transmitter positions from both parents randomly at 1:1 ratio
```

cases indicates most of the transmitters should be positioned around the center of the panel, as we have observed from the randomly generated sets. As vibrational effect tends to introduce higher combined pointing error angle, transmitters being around the center makes it more convenient for the receiving end to capture most of the energy even at the presence of vibrations using this tiling pattern. Later, we determine the best positions of the transmitter positions after 150 generations and shown in Fig. 5.12(a) and 5.12(b). Both of these tiling solutions indicates optimum transmitter positions to obtain best *SINR* performance under vibrational effects. Comparing the solutions of the genetic algorithm with the solution from randomly generated cases shown in Fig. 5.10(b), we establish that we can obtain the optimized tiling solution using the genetic algorithm approach utilizing much smaller computational capability.

Table 5.1: Summary of Genetic Algorithm Simulations

Fit Population size	# of Generations to Converge	Peak SINR (dB)
20%	190	24.09
10%	145	24.06
5%	100	24.03
1%	80	23.96

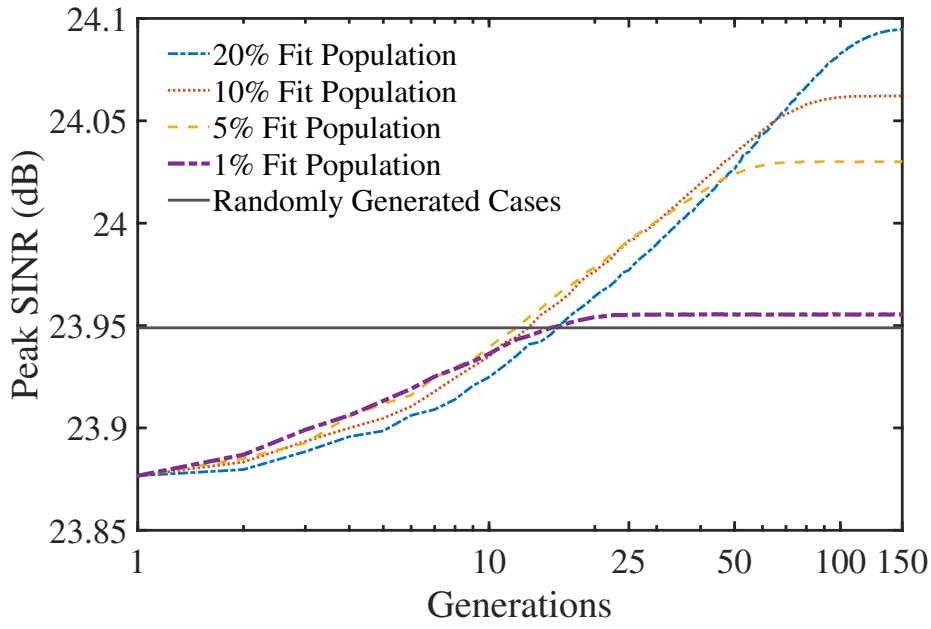

(a)

Figure 5.13: Peak SINR of the fit population over 150 generations of evolution.

To understand the effect of the genetic algorithm parameters on the results, we varied the fit population size and observed *SINR* over generations. To determine how many generations it requires to achieve the *SINR* saturation, we vary the fit population size for different values from 20% to 1%. All every cases, total population size of a generation was fixed at $5,000$ and number of transmitters, $N = 2200$. Figure 5.13 shows variation of the peak *SINR* of the fit populations over generations. As shown in Fig. 5.13, smaller fit population yields better solutions in early generations but converges

to a more sub-optimal solution eventually. However, we can achieve best *SINR* performance when the fit population is increased. Essentially this requires generating more generations and computational time. We summarized the results from the genetic algorithm simulations in Table 5.1. In both Fig. 5.13, we inserted a grey solid line that indicated the value from randomly generated sets. We can clearly observe genetic algorithm approach consistently outperforms the randomized set selection after about 20 generations.

In summary, we have outlined a model for optimizing the tiling positions for multi-element transceiver design. We developed a simulation tool in MATLAB to determine the best performance for optimizing communication throughput even under the presence of vibrational effect of the mobile platform. We explored randomly generated sets and Genetic Algorithm approach to optimize the tiling of optical elements within the square transceiver plane. Furthermore, the optimum solution achieved through the developed algorithm can be extended for dynamic solutions and various shapes and sizes of the transceiver.

CHAPTER 6: DEFOCUSED LENS ASSEMBLY DESIGN FOR MULTI-ELEMENT FULL-DUPLEX FSO TRANSCEIVER

In this chapter, we address the issues of establishing a LOS optical link between mobile platforms such as UAVs, autonomous vehicle, floating base-stations, and stationary building top transceivers, as shown in Fig. 6.1. We propose a near-afocal lens assembly design for multi-element FSO transceiver to optimize the received power based on link distance and transceiver layout design. The main contributions in this chapter are as follows:

- An optimized design of multi-element FSO transceiver layout that includes selecting number of transmitters and receivers and placement of the elements within the transceiver plane.
- An overview of the circuit design considerations taken into account to implement the FSO transceiver for deployment.
- A defocal lens assembly design for the transmitters to control the beam width and beam footprint at the receiver end to optimize the received power and tolerance to vibration, sway, and tilt of the mobile platform.

6.1 Multi-Element Full-Duplex FSO Transceiver: Theoretical Background

In this section, we will present the design methodology and tiling of the elements on the transceiver plane to optimize performance, such as IBFD communication throughput. We used optimization technique to find the optimum number of transmitters and utilized genetic algorithm to tile those in a fashion that gives uninterrupted performance even in the presence of vibration.

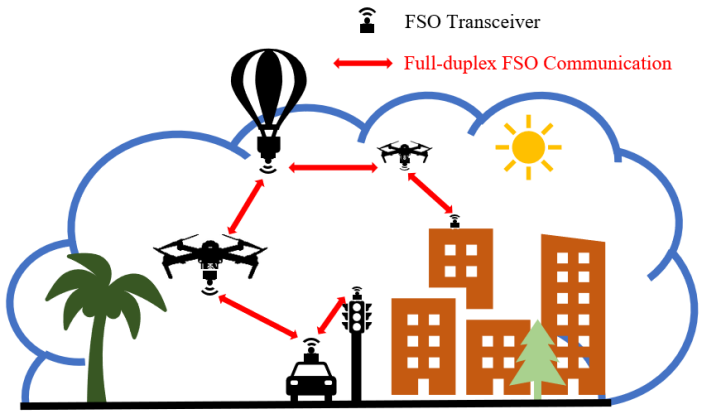

Figure 6.1: Full-duplex FSO communication between mobile nodes.

6.1.1 Layout Optimization by Tiling

To determine the optimum transceiver layout, we developed a MATLAB simulation tool to characterize the optical link by incorporating beam characteristics and propagation losses, such as atmospheric turbulence and self-interference. For this simulation, we used 50 m long FSO channel between two UAVs communicating in IBFD mode using wavelength λ = 900 nm. The transceiver size is set to 10 cm $\times$ 10 cm.

SINR characterizes the quality of a communication system as well as it is the performance parameter for a transceiver. Considering an FSO link established using transceivers A and B, each with a single transmitter having a divergence angle of θ and a single receiver having a detection area of A_{det}, SINR can be written for node A as [74]

$$SINR_A = \left[\frac{P_B L_z(d,\lambda) A_{det} \cos(\phi \pm \delta)}{(\tan\theta)^2 4d^2 (N_T + \Gamma_{SA})}\right]^2, \tag{6.1}$$

where P_B is the transmit power at node B, d is the link distance, and $L_z(d,\lambda)$ is the free-space loss parameter for a link distance of d. ϕ is the pointing error angle when the transceivers are perfectly

aligned, and δ is the 'vibration angle' which is the additional pointing error due to vibration on the mobile transceivers.

For a multi-element FSO transceiver with N transmitters having θ divergence angle each and m receivers with detection area of A_{det}, SINR for node A can be expressed as

$$SINR_A = \sum_{i=1}^{N} \sum_{j:j\in\mathscr{F}_i} \left[\frac{P_{B,i} L_z(d,\lambda) A_{det} \cos(\phi_j \pm \delta_j)}{(\tan\theta)^2 4d^2 (N_T + \Gamma_{SA})} \right]^2, \tag{6.2}$$

where i and j denote the index of transmitter and receiver, respectively. $P_{B,i}$ denotes the transmit power at transmitter i at node B. Each transmit beam projects a beam footprint on the transceiver plane and only covers a subset of the available receivers in a transceiver. $\mathscr{F}_i$ represents the set of receivers that falls within the beam footprint of transmitter i. ϕ_j and δ_j are the pointing error and the vibration angles on the beam arriving at receiver $j \in \mathscr{F}_i$.

To determine the number of the transmitters required to optimize the layout design, we simulated the FSO link by varying the transmitter count. As the position and count of the transmitter are varied, a pointing loss add to the overall loss parameters. This additional loss degrades the performance of the optical link. We further investigated the link performance based on transmit power and divergence angle of the transmitter to observe the variation on link performance parameter, eg. signal to interference and noise ratio (SINR). Based on the simulation, we observe that the SINR of the optical link is highest when 22% of the transceiver area is used as transmitter and 78% area is dedicated for receivers [52].

To determined the optimum position of the transmitters, we devised a genetic algorithm approach with smaller segment area. We divided the transceiver plane into 100×100 smaller segments and assigned 22% of the segments as transmitter. In our developed algorithm, we have randomly generated $5,000$ different sets by placing the transmitters in different segments to start the process.

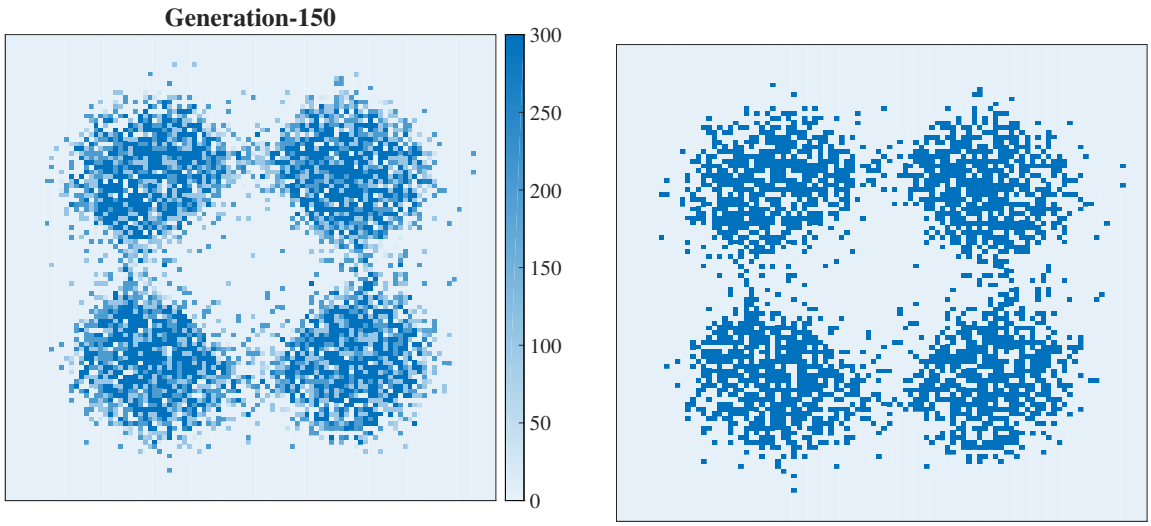

Figure 6.2: (a) Heatmap of transmitter locations, and (b) optimized transmitter locations on a 100×100 transceiver grid using genetic evolution after generation 150 with 20% fit population with vibrational effect.

After calculating the SINR for each sets, we selected best 10% of the sets, which we named 'fit population'. We used these fit population sets to generate the population of $5,000$ sets for the next generation by crossover technique. This process of generating population set and calculating SINR to determine fit population for the next generation is iterated until we achieve the best optical link performance. Once we converge to a solution, we can generate a heatmap of the optimized 'fit population' to determine the locations where we place the transmitters, as shown in Fig. 6.2. The converged heatmap shows that the transmitter locations are more clustered in four lobes located midway towards the corners of the transceiver plane from the center.

6.1.2 Circuit Design for Transmitter and Receiver Threads

We discuss about the circuit design considerations for the 10×10 transceiver prototype for multi-element FSO link by incorporating SWaP constraints [52]. The electrical circuit associated with

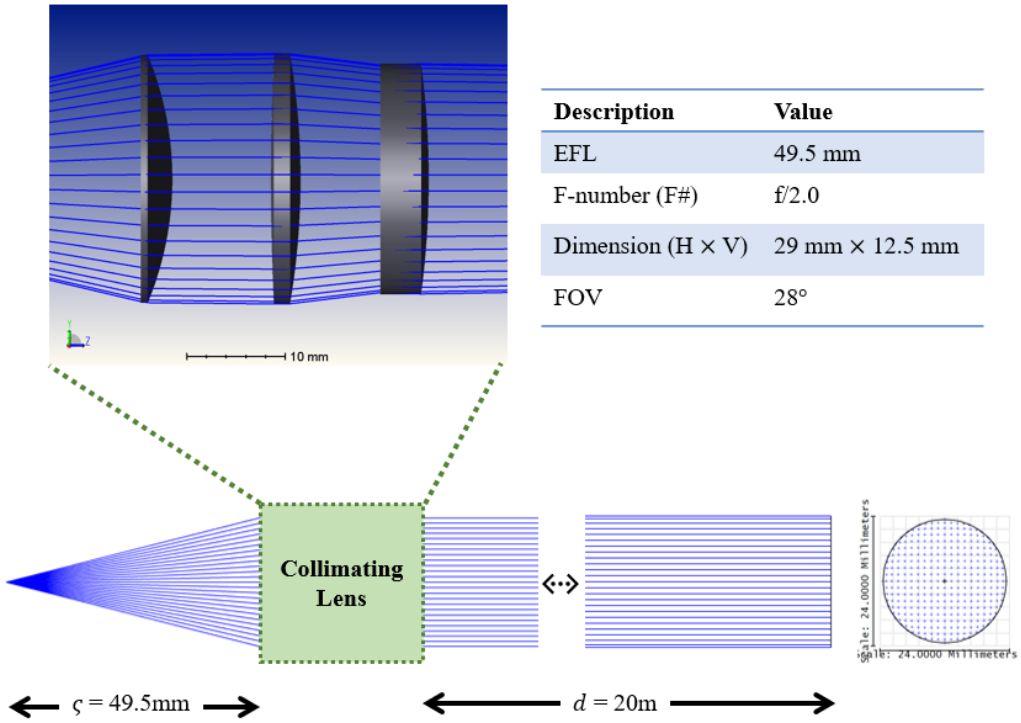

Description	Value
EFL	49.5 mm
F-number (F#)	f/2.0
Dimension (H × V)	29 mm × 12.5 mm
FOV	28°

Figure 6.3: Fixed effective focal length lens for FSO system.

the transmitter and receiver thread are designed separately. However, both of the circuits interact with the controller and laid out on the same printed circuit board (PCB) in accordance to the layout simulated in the previous section.

As shown in previous section, the optical simulation provides best link performance if there are 22 transmitters in the 10×10 transceiver array. However, to distribute the transmitter along multiple routes and balance the current supplied to each transmitter, we choose to use 24 transmitters. The transmitters are clustered in 4 areas as shown in Fig. 6.2, having 6 transmitters in each cluster. In our circuit, we distributed 3 transmitters per path and defined 8 paths for transmit thread. The combination of all the transmitting elements' aggregate power will give a better SNR for the receiving end. The second reason why the 8×3 layout was chosen due to voltage and current driving requirements of the transmitter circuit elements (narrow band LEDs).

For the receiver circuit design, the baseline layout was chosen roughly 10×10. This routing path is chosen for three reasons: First, it is easier for routing to one path per column, with more or less elements per path as needed to match the array. Second, the RC delay the elements may deteriorate the received signal. However, allowing multiple path to dissipate the accumulated charges for the receiver elements ensures each bit is received without any residual charges in the circuit. Third, the overall capacitance of the circuit remains relatively low if we combine the components in series and parallel combination and we can control the effective capacitance of the receiver circuit. The detail design, circuit diagram, and performance analysis by considering SWaP constraints are presented in our previous work [52].

6.2 Defocal Lens Assembly for Transmitters

When parallel (or collimated) light rays from an infinitely distant source falls on a lens system, there are three possible outcomes: first, the parallel rays converge to a real-point outside the lens system, second, the light rays appears to diverge from a point within the lens system, and third, they emerge as parallel (or collimated) rays after the lens system with a little different characteristics compared to the incident rays. In the first two cases, the lens system has a finite focal length and field-of-view (FOV). These systems are called focal systems. On the other hand, the system in the third case does not have finite focal length, or one can say the light rays converge or diverge at a infinite length. This system is called afocal lens system. The direction of the ray path is reversible. Hence, for the first case scenario, if a diverging point source is place at a focal length of a lens system, the output light rays appears to be parallel (or collimated), as shown in Fig. 6.3. We utilize this characteristics to design a lens assembly for the transmitters for medium range FSOC.

To improve the performance of the overall optical system, one of the major parameter that requires improvement is optical coupling efficiency (η_{OC}). The expression for η_{OC} can be given as follows

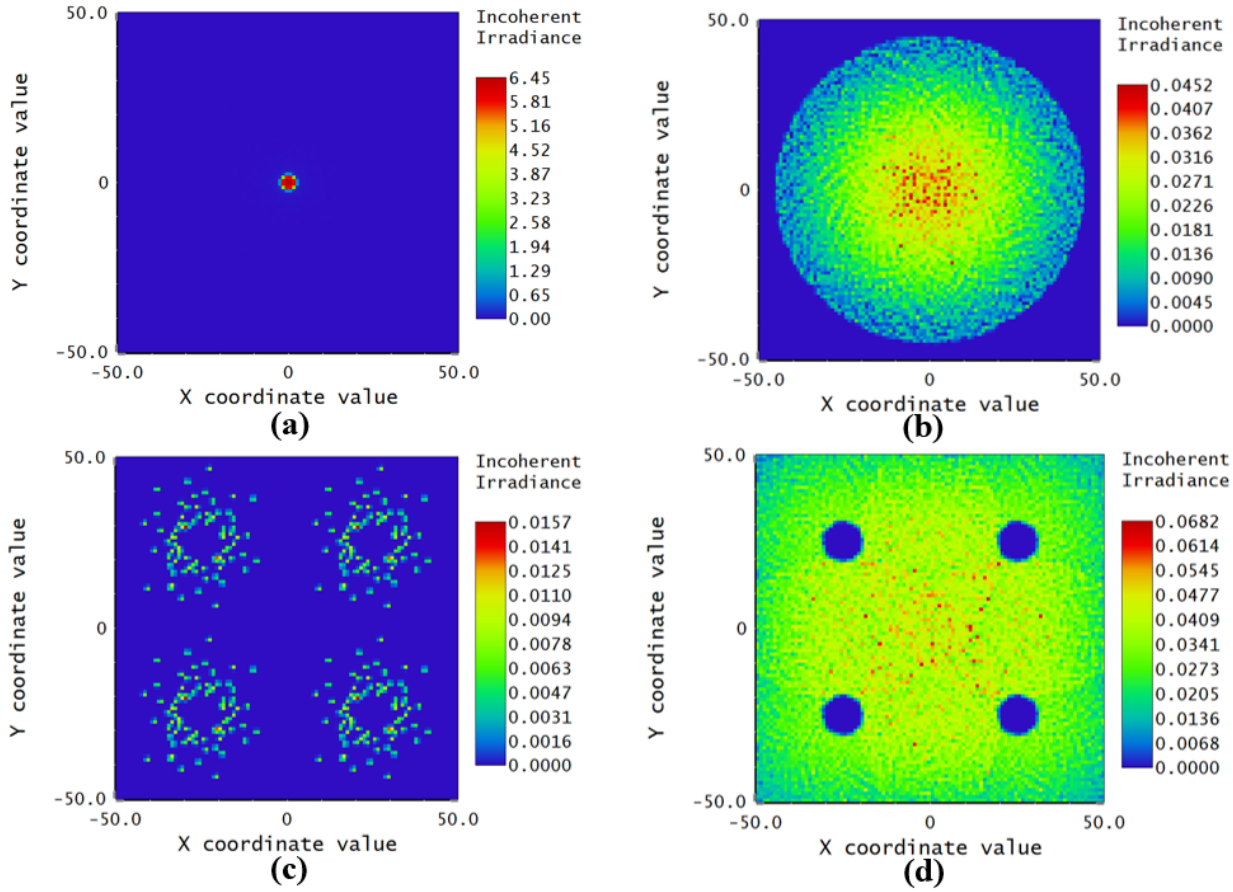

Figure 6.4: Optical beam footprint for (a) single transmitter collimated beam ($\Delta\zeta = 0$), (b) single transmitter defocused beam ($\Delta\zeta = 0.8$ mm), (c) four transmitters collimated beam ($\Delta\zeta = 0$), and (d) four transmitters defocused beam ($\Delta\zeta = 0.8$ mm).

$$\eta_{OC} = \eta_T \eta_{ch} \eta_R, \tag{6.3}$$

where η_R is the transmitter outcoupling efficiency, η_{ch} is the channel coupling efficiency tht includes atmospheric attenuation losses and purtubations, and η_R is the receiver efficiency that includes power collected by the receiver area and coupling optical power into electrical circuits. Losses incurred during the beam propagation through free-space are accounted for in the coupling term η_{ch}. Atmospheric absorption, scattering, and turbulence are the major factors to deteriorate

beam quality and directionality. However, these effects are minimum when we consider clear weather, higher visibility, and temperature gradient is small. These effects may become prominent for long-range FSOC [89].

In paraxial analysis, the transmitter is placed at the focal point of the lens system on the optical axis. If the emission distribution is described by $J_T(\beta)$, where J_T is normalized to emission into 2π steradians of a hemisphere and β is the angle from zenith. The transmitter then can be approximated by [90]

$$\eta_T = \int_0^{\beta_{max}} \int_0^{2\pi} J_T(\beta) d\beta d\phi, \tag{6.4}$$

where $\beta_{max} = \tan^{-1}(1/2F_T)$ is the angle of the marginal rays to the edge of the lens and F_T is the F-number of the lens. The coupling efficiency of the receiver (η_R) can be described as the fraction of power collected by the receiver that arrive to the receiver plane. If the intensity distribution of the beam at the receiver plane is defined as $J_R(d)$, η_R can be given by

$$\eta_R = \frac{\int\int \Big(J_R(d) \circledast A_R \Big)}{\int\int \Big(J_R(d) \circledast A_{BF} \Big)}, \tag{6.5}$$

where d is the optical link distance, A_R is the effective receiver area, and $A_{BF} =$ is the beam footprint at the transceiver plane. This coupling efficiency cannot be represented by the ratio of the receiver area and beam footprint, as the intensity of a Gaussian beam varies within the beam cross section.

To observe the relation between the optical link distance, coupling efficiency, defocused beam footprint, and vibration tolerance, we developed a lens assembly in Zemax OpticStudio with paraxial approximation. The lens assembly was designed in a fashion so that the light rays coming out of the lens are collimated and hence can be useful for longer optical range. The lens prescription was optimized using sequential mode in Zemax. The spot size of the beam on the receiver plane is 11

mm and most of the power is contained within the beam width, as shown in Fig. 6.4(a). But if we consider transceiver design, this beam will fall only on the transmitter on the other side and none of the power arriving at the receiver plane will be converted into signal. Hence, we deliberatley defocus the beam by changing the distance (ζ) between transmitter and lens assembly. A very small offset of $\Delta\zeta = 0.8$ mm can lead to a much bigger beam footprint at the receiver plane, as shown in 6.4(b). Now, as outlined in previous section, we have four cluster of transmitters on the transceiver plane. We simulated the transceiver plane power coupling by using non-sequential environment in Zemax. For both collimated (Fig. 6.4(c)) and defocused (Fig. 6.4(d)) cases, beam footprint shows how much power would be coupled into the receiver.

6.3 Results and Discussion

We present a defocused lens system for the transmitter of the laser-based FSOC link. We designed a fixed focal length lens system with adjustable distance between transmitter and lens assembly (ζ). The adjustable ζ can be effective and advantageous for three reasons: First, the controller can optimize the beam footprint radius by implementing feedback algorithm so that it can cover maximum receiving area and couple maximum power to the receiving end. Second, with the variation of optical link range, defocusing distance ($\Delta\zeta$) is different. The adjustability of the $\Delta\zeta$ gives a optimum operating condition over a wide window of optical range. Third, mobile platforms tend to experience loss of communication due to vibration, sway, and tilt. Use of lasers as transmitters makes it even harder to maintain the optical link. By using adjustable $\Delta\zeta$, we can provide robustness and tolerance to vibration and sway. However, this robustness to vibrations comes with a trade-off. We can increase tolerance by increased defocus and larger beam footprint, which leads to distributed intensity and lower coupling efficiency. We define a term (ξ) to measure the trade-off between beam footprint radius (R) and coupling efficiency (η_{OC}), where $\xi = R \times \eta_{OC}$.

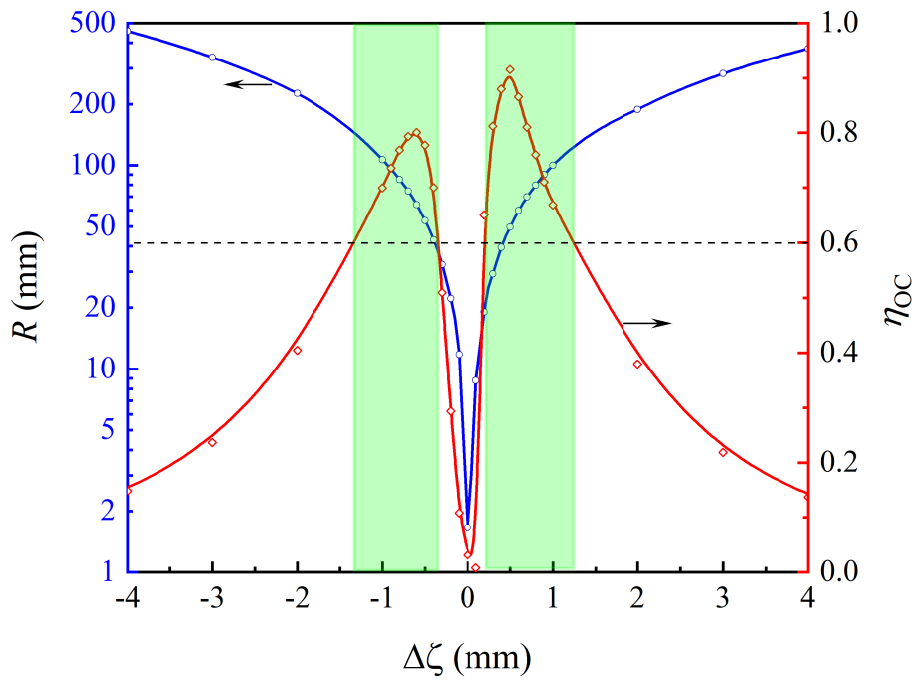

Figure 6.5: Beam width radius, R, (blue line) and optical coupling efficiency, η_{OC}, (red line) for optical link range, $d = 20$ m.

We start our design by optimizing the lens assembly, defined in Fig. 6.3, in the sequential environment in Zemax. We determine the beam footprint radius (R) of the beam spot on the receiver plane. As we can see from Fig. 6.5, the radius increases with the defocusing distance ($\Delta\zeta$) for a link distance of $d = 20$ m and corresponding ray trace diagram is also shown in Fig. 6.3. The corresponding vibration tolerance margin is also calculated and shown in Fig. 6.6. The tolerance of the system in terms of the defocusing distance corresponds to the beam footprint diagram. If we track the area covered by the beam footprint (area enclosed by dotted green box in Fig. 6.6 inset), the additional length in either horizontal or vertical direction represents the tolerance length.

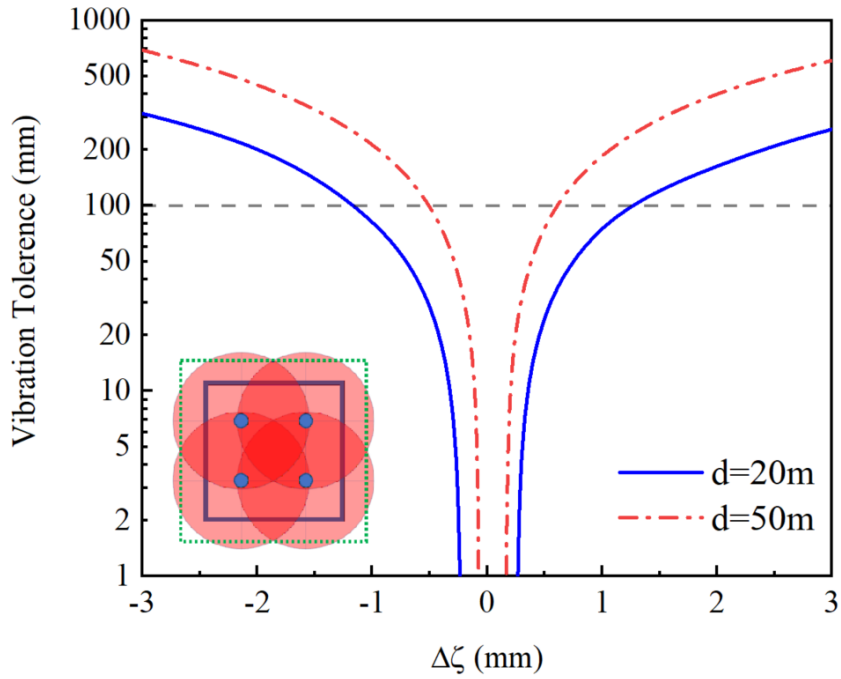

Figure 6.6: Vibration tolerance for defocused lens system for $d = 20$ m and $d = 50$ m.

After we finalize the lens system design based on the collimation of light rays, we convert our lens design into non-sequential environment. Based on the our simulation results presented in previous section, we position four (4) transmitters on the transceiver plane and rest of the area is defined as receiver. The distance between two transceiver planes is varied from 20 m to 75 m. The coupling efficiency is calculated based on the received power by the receiver. Figure 6.5(red line) shows the coupling efficiency with respect to defocusing distance ($\Delta\zeta$). As expected when, $\Delta\zeta = 0$ or the incoming beam to the receiver plane is collimated, least amount of power is coupled into receiver, as most the power is perfectly aligned with the transmitter on the transceiver plane. But as the defocusing starts to kick in, coupled received power also increases as long as the beam radius falls within the transceiver plane. When the beam radius at the receiver plane becomes significantly larger than transceiver area, coupling efficiency goes down again. Even

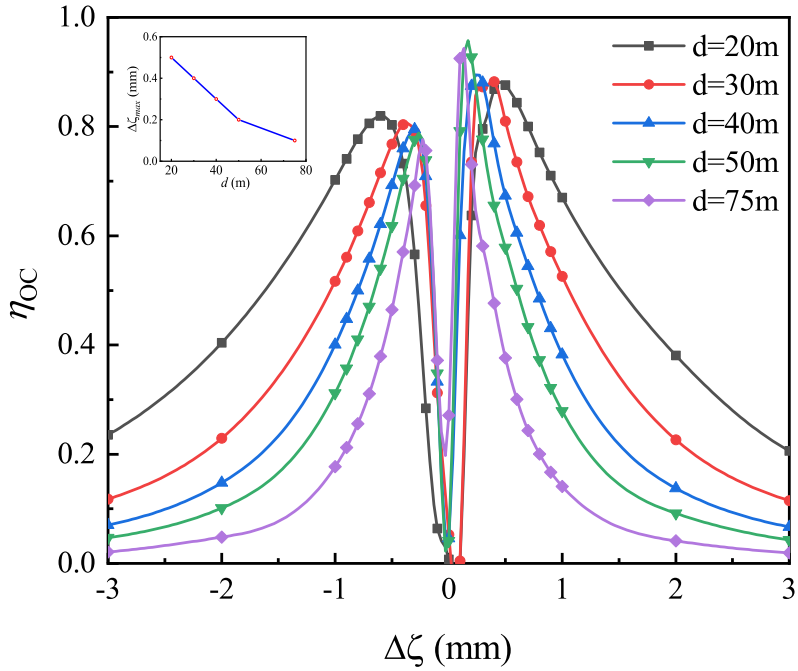

Figure 6.7: Optical coupling efficiency, η_{OC}, for different link range, d. Inset: Defocused length ($\Delta\zeta_{max}$) corresponding to the maximum coupling effieicny for different link range, d.

though Gaussian beam concentrates more power at the center of the beam cross-section, as the beam radius increases, power starts to distribute over larger area and effective coupling goes down. We further investigate the effect of optical link range (d) on the coupling efficiency. The maximum coupling efficiency (η_{max}) remains relatively constant over wide window of optical range (from 20 m to 75 m). However, η_{max} occurs at different defocusing distance ($\Delta\zeta_{max}$) for different d values. Figure 6.7 shows the coupling efficiency for different d values at different $\Delta\zeta$ positions. We have also shown how the position of $\Delta\zeta_{max}$ varies for over a window of optical link range.

Finally we calculate the value of ξ to determine the optimum operating defocusing distance, $\Delta\zeta$. Figure 6.8 shows the trade=off parameter, ξ, with respect to $\Delta\zeta$ for different optical link range, d. We can determine the value of optimum value of $\Delta\zeta_{opt}$ from these plots. We can observe that

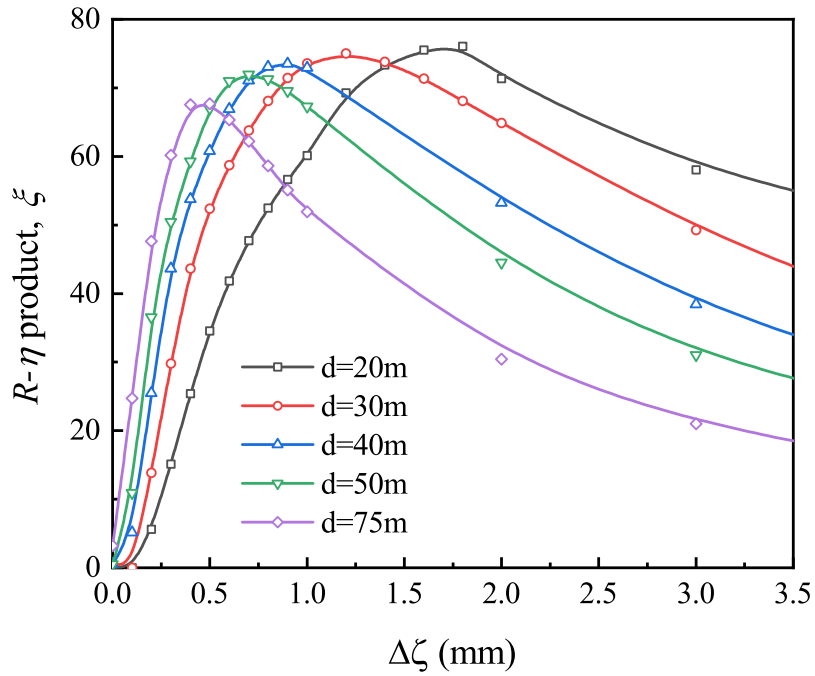

Figure 6.8: Variation of trade-off parameter, ξ, corresponding to defocused length, $\Delta\zeta$ for different optical link range, d.

$\Delta\zeta_{opt}$ is smaller for higher d values, as non-collimated beam has larger beam footprint for longer link range. As a result, coupling efficiency drops much faster compared to smaller link range, as can be observed from Fig. 6.7 as well. These simulation results provide a guideline for designing fixed effective focal length lens system and how defocusing can be utilized to optimize coupling efficiency and vibration tolerance for a mobile FSOC link.

In summary, we presented a complete design guideline for full-duplex FSO transceiver for short to medium range mobile FSOC link. We incorporated atmospheric attenuation and turbulence effect in designing a multi-element FSO transceiver, which shows maximum SINR performance with 22% of the transceiver area is used for transmitters when transmitters are placed in an equi-distance circular pattern from the center. We generated a layout for optimum performance by

using genetic algorithm. We outlined how these multiple optical elements, namely transmitters and receivers, are connected in the electrical circuit by considering SWaP constraints. And finally, we developed a transmitter lens assembly with fixed effective focal length to maximize the optical coupling efficiency and vibration tolerance for a mobile FSOC link by adjusting defocusing length. We proposed a lens system with 49.5 mm EFL, F/2, and FOV of 28° for each transmitter cluster which gives a coupling efficiency of upto 57% and vibration tolerance of 11.5 cm when the link range is $d = 50$ m.

CHAPTER 7: CONCLUSION

In conclusion, we modeled the effect of atmospheric attenuation and corresponding link length for an in-band full-duplex optical transceiver design in various cases. We considered the effects of passive and active SI suppression, and also how performance of the optical channel can be improved or made immune to SI by taking into account the design parameters, such as transmit power and receiver positioning. We proposed a mathematical model for passive SIC by isolation technique. We calculated background noise and residual SI power to measure the performance of the channel by calculating SINR of the communication link. We observed that even with high visibility ($V \geq 1$ km), link length of the free-space optical channel is limited to ≈ 120 m when the distance between the transmitter and the receiver of the full-duplex transceiver is 5 cm. We also presented the performance of the channel based on the SI suppression level (δ).

We also presented a proof-of-concept prototype of an IBFD-FSO transceiver. We isolated the transmitter and receiver of a node using a cover to prevent optical feedback. Through real test-bed experiments, we demonstrated that, using the IBFD-FSO transceiver, in-band full-duplex operation can be successfully performed. We observed that, when the surface where the transceiver is placed is not black, reflection causes optical feedback. This can be prevented by either using a black surface or placing the transceiver at a suitable height from a reflecting surface. Also, the current prototype was built using off-the-shelf components. We were limited by the IrDA2 Click's maximum range of 2.75 m, divergence angle of 24° and maximum UART speed of 115.2 Kbps. Moreover, the distance between the transmitter and the receiver of a node was 1.9 cm when they were placed next to each other, and 3.2 cm when they were placed on top of each other.

We demonstrated that two UAVs can discover each other by mechanically steering their IBFD directional transceivers using an asynchronous discovery protocol by performing real test-bed ex-

periments. We demonstrated that by randomly selecting angular speed and initial scan position, the LOS link can be established between two UAVs within a limited time period. The experiments for improving the discovery time by resetting angular scan speed after a threshold time (t_{reset}) is still in progress. Another promising line of future work is to extend the capabilities of the algorithm beyond discovery phase into the maintenance phase, where the established LOS can be maintained even the aerial nodes are in motion and within communication range.

We have outlined a model for optimizing the tiling position for multi-element transceiver design. We have incorporated weather effect and SI that arise within a transceiver unit to obtain a design model for simulating in-band full-duplex FSO channel. A simulation tool is developed in MATLAB to determine the best performance for optimizing communication throughput even under the presence of vibrational effect of the mobile platform. We presented that for a transceiver plane consisting 10×10 grid size, the best performance can be achieved for $N = 22$. Later, we extended that tiling technique to 100×100 grid with 22% area covered by transmitters. We explored randomly generated sets to explore the optimum solution, however, complexity of the problem makes it difficult to reach optimum solution. We also implemented a Genetic Algorithm technique to optimize the tiling positions. We presented a guideline for positioning the transmitters within transceiver plane using both approaches. The model can be further improved by including sway and tilt of the transceiver platform and by considering multi-channel link design where inter-symbol interference plays additional role on the performance of the aggregated link. Also, optimizing transmit power (P_i) for each transmitter and dynamic optimization of transmitter count (N^*) during genetic algorithm can be investigated as future study.

We explored the design and analysis of a fixed effective focal length lens system and the optical coupling efficiency can be maximized by defocusing the beam footprint on the receiver side for a full-duplex free-space optical communication link. We proposed a lens system with effective focal length of 49.5 mm, F/2, and FOV of 28° to collimate transmit beam on to the receiver plane.

We further presented how to maximize the optical coupling efficiency and vibration tolerance by introducing small defocusing length between transmitter and lens assembly. Our proposed lens system gives a coupling efficiency of upto 57% and vibration tolerance of 11.5 cm when the link range is $d = 50$ m.

Some of the future work directions for this research includes:

- A multi-element transceiver design by tiling optical elements, such as transmitters and receiver, on the transceiver plane. An analytical model of link performance parameter, SINR, is to be developed for multi-element full-duplex FSO transceiver by considering free-space attenuation as well as the vibration model of the mobile platform, e.g., an unmanned aerial vehicle (UAV). We will explore an optimized approach of tiling elements within transceiver plane by implementing genetic algorithm and evaluating multiple generations of solutions to reach the most favorable tiling pattern.

- We plan to improve the performance of the prototype in terms of data rate and link range by using VCSEL-based transmitter and high-speed photodiodes as receiver.

- A 2D maintenance algorithm will be implemented to keep the link up by changing the direction and angular velocity of the two mounted transceivers based on the speed and direction of our vehicles. We will show that maintenance of FSOC links can be achieved between two autonomous mobile vehicles using laser-based full-duplex transceivers.

- We plan to extend the maintenance algorithm to 3D space and integrate to the discovery algorithm to realise mobile FSO communication between two aerial nodes.

LIST OF REFERENCES

[1] I. K. Son and S. Mao, "A survey of free space optical networks," *Digital communications and networks*, vol. 3, no. 2, pp. 67–77, 2017.

[2] A. Sevincer, M. Bilgi, and M. Yuksel, "Automatic realignment with electronic steering of free-space-optical transceivers in MANETs: A proof-of-concept prototype," *Ad Hoc Networks*, vol. 11, pp. 585–595, January 2013.

[3] M. Khan, M. Yuksel, and G. Winkelmaier, "GPS-free maintenance of a free-space-optical link between two autonomous mobiles," *IEEE Transactions on Mobile Computing*, vol. 16, no. 6, pp. 1644–1657, 2017.

[4] M. Khan and M. Yuksel, "Autonomous alignment of free-space-optical links between UAVs," in *Proceedings of the 2nd International Workshop on Hot Topics in Wireless*, pp. 36–40, ACM, 2015.

[5] "Facebook laser communication." https://www.facebook.com/zuck/videos/10102274951725301/.

[6] X. Xie and X. Zhang, "Does full-duplex double the capacity of wireless networks?," in *INFOCOM*, IEEE, 2014.

[7] S. Goyal, P. Liu, O. Gurbuz, E. Erkip, and S. Panwar, "A distributed MAC protocol for full duplex radio," in *Signals, Systems and Computers, 2013 Asilomar Conference on*, pp. 788–792, IEEE, 2013.

[8] Z. Zhang and B. Li, "Neighbor discovery in mobile ad hoc self-configuring networks with directional antennas: Algorithms and comparisons," *IEEE Transactions on Wireless Communications*, vol. 7, no. 5, 2008.

[9] E. Everett, M. Duarte, C. Dick, and A. Sabharwal, "Empowering full-duplex wireless communication by exploiting directional diversity," in *Signals, Systems and Computers (ASILOMAR), 2011 Conference Record of the Forty Fifth Asilomar Conference on*, pp. 2002–2006, IEEE, 2011.

[10] E. Everett, A. Sahai, and A. Sabharwal, "Passive self-interference suppression for full-duplex infrastructure nodes," *IEEE Transactions on Wireless Communications*, vol. 13, no. 2, pp. 680–694, 2014.

[11] K. Wang, A. Nirmalathas, C. Lim, and E. Skafidas, "Experimental demonstration of full-duplex optical wireless personal area communication system with 16-CAP modulation," in *Optical Fiber Communications Conference and Exhibition (OFC), 2015*, pp. 1–3, IEEE, 2015.

[12] K. Wang, A. Nirmalathas, C. Lim, K. Alameh, and E. Skafidas, "Full-duplex gigabit indoor optical wireless communication system with CAP modulation," *IEEE Photonics Technology Letters*, vol. 28, no. 7, pp. 790–793, 2016.

[13] P. Zhang, Y. Lou, T. Wang, G. Yang, L. Zhang, S. Tong, and H. Jiang, "Link budget and simulation of double-wavelength full-duplex free-space laser communication based on modulating retro-reflector," in *Wireless Communications, Networking and Applications*, Springer, 2016.

[14] B. E. Johnson, T. A. Lindsay, D. L. Brodeur, R. E. Morton, and M. A. Regnier, "Wide-angle, high-speed, free-space optical communications system," Oct. 25 1994. US Patent 5,359,446.

[15] A. Sevincer, M. Bilgi, and M. Yuksel, "Automatic realignment with electronic steering of free-space-optical transceivers in MANETs: A proof-of-concept prototype," *Ad Hoc Networks*, vol. 11, pp. 585–595, January 2013.

[16] E. J. Mayeux, "Optical transceiver for free-space communication links," Feb. 14 1995. US Patent 5,390,040.

[17] D. Weatherington and U. Deputy, "Unmanned aircraft systems roadmap, 2005-2030," *Deputy, UAV Planning Task Force, OUSD (AT&L)*, 2005.

[18] F. R. Gfeller and U. Bapst, "Wireless in-house data communication via diffuse infrared radiation," *Proceedings of the IEEE*, vol. 67, no. 11, pp. 1474–1486, 1979.

[19] Z. Ghassemlooy, W. Popoola, and S. Rajbhandari, *Optical wireless communications: system and channel modelling with Matlab®*. CRC press, 2019.

[20] N. Saeed, H. Almorad, H. Dahrouj, T. Y. Al-Naffouri, J. S. Shamma, and M.-S. Alouini, "Point-to-point communication in integrated satellite-aerial 6g networks: State-of-the-art and future challenges," *IEEE Open Journal of the Communications Society*, 2021.

[21] H. Gu, K. Chen, Y. Yang, Z. Chen, and B. Zhang, "Mronoc: A low latency and energy efficient on chip optical interconnect architecture," *IEEE Photonics Journal*, vol. 9, no. 1, pp. 1–12, 2017.

[22] B. Patnaik and P. K. Sahu, "Inter-satellite optical wireless communication system design and simulation," *IET Communications*, vol. 6, no. 16, pp. 2561–2567, 2012.

[23] A. Sabharwal, P. Schniter, D. Guo, D. W. Bliss, S. Rangarajan, and R. Wichman, "In-band full-duplex wireless: Challenges and opportunities," *IEEE Journal on Selected Areas in Communications*, vol. 32, no. 9, pp. 1637–1652, 2014.

[24] D. Kim, H. Lee, and D. Hong, "A survey of in-band full-duplex transmission: From the perspective of PHY and MAC layers," *IEEE Communications Surveys & Tutorials*, vol. 17, no. 4, pp. 2017–2046, 2015.

[25] J. I. Choi, M. Jain, K. Srinivasan, P. Levis, and S. Katti, "Achieving single channel, full duplex wireless communication," in *Proceedings of the sixteenth annual international conference on Mobile computing and networking*, pp. 1–12, ACM, 2010.

[26] D. Kim, S. Park, H. Ju, and D. Hong, "Transmission capacity of full-duplex-based two-way ad hoc networks with ARQ protocol," *IEEE Transactions on Vehicular Technology*, vol. 63, no. 7, pp. 3167–3183, 2014.

[27] M. Jain, J. I. Choi, T. Kim, D. Bharadia, S. Seth, K. Srinivasan, P. Levis, S. Katti, and P. Sinha, "Practical, real-time, full duplex wireless," in *Proceedings of the 17th annual international conference on Mobile computing and networking*, pp. 301–312, ACM, 2011.

[28] M. Duarte, A. Sabharwal, V. Aggarwal, R. Jana, K. Ramakrishnan, C. W. Rice, and N. Shankaranarayanan, "Design and characterization of a full-duplex multiantenna system for WiFi networks," *IEEE Transactions on Vehicular Technology*, vol. 63, no. 3, pp. 1160–1177, 2014.

[29] Y. Wang, Y. Wang, N. Chi, J. Yu, and H. Shang, "Demonstration of 575-Mb/s downlink and 225-Mb/s uplink bi-directional SCM-WDM visible light communication using RGB LED and phosphor-based LED," *Optics express*, vol. 21, no. 1, pp. 1203–1208, 2013.

[30] C. W. J. Oh, Z. Cao, E. Tangdiongga, and T. Koonen, "10 Gbps all-optical full-duplex indoor optical wireless communication with wavelength reuse," in *OFC*, pp. Th4A–6, Optical Society of America, 2016.

[31] A. K. Majumdar, "Free-space laser communication performance in the atmospheric channel," *Journal of Optical and Fiber Communications Reports*, vol. 2, no. 4, pp. 345–396, 2005.

[32] A. Al-Habash, L. C. Andrews, and R. L. Phillips, "Mathematical model for the irradiance probability density function of a laser beam propagating through turbulent media," *Optical Engineering*, vol. 40, no. 8, pp. 1554–1563, 2001.

[33] F. S. Vetelino, C. Young, and L. Andrews, "Fade statistics and aperture averaging for Gaussian beam waves in moderate-to-strong turbulence," *Applied optics*, vol. 46, no. 18, pp. 3780–3789, 2007.

[34] S. S. Muhammad, P. Kohldorfer, and E. Leitgeb, "Channel modeling for terrestrial free space optical links," in *Transparent Optical Networks, 2005, Proceedings of 2005 7th International Conference*, vol. 1, pp. 407–410, IEEE, 2005.

[35] H. E. Nistazakis, E. A. Karagianni, A. D. Tsigopoulos, M. E. Fafalios, and G. S. Tombras, "Average capacity of optical wireless communication systems over atmospheric turbulence channels," *Journal of Lightwave Technology*, vol. 27, no. 8, pp. 974–979, 2009.

[36] K. P. Peppas, A. N. Stassinakis, G. K. Topalis, H. E. Nistazakis, and G. S. Tombras, "Average capacity of optical wireless communication systems over IK atmospheric turbulence channels," *IEEE/OSA Journal of Optical Communications and Networking*, vol. 4, no. 12, pp. 1026–1032, 2012.

[37] "Project loon." https://x.company/loon/.

[38] R. W. DeVaul, E. Teller, C. L. Biffle, and J. Weaver, "Establishing optical-communication lock with nearby balloon," Jan. 9 2012. US Patent App. 13/346,645.

[39] R. DeVaul, E. Teller, C. Biffle, and J. Weaver, "Using predicted movement to maintain optical-communication lock with nearby balloon," Dec. 17 2013. US Patent App. 14/108,542.

[40] R. R. Choudhury, X. Yang, R. Ramanathan, and N. H. Vaidya, "On designing mac protocols for wireless networks using directional antennas," *IEEE Transactions on Mobile Computing*, vol. 5, no. 5, 2006.

[41] X. An and R. Hekmat, "Self-adaptive neighbor discovery in ad hoc networks with directional antennas," in *Mobile and Wireless Communications Summit, 2007. 16th IST*, pp. 1–5, IEEE, 2007.

[42] R. Ramanathan, J. Redi, C. Santivanez, D. Wiggins, and S. Polit, "Ad hoc networking with directional antennas: a complete system solution," *IEEE JSAC*, vol. 23, no. 3, pp. 496–506, 2005.

[43] G. Pei, M. M. Albuquerque, J. H. Kim, D. P. Nast, and P. R. Norris, "A neighbor discovery protocol for directional antenna networks," in *IEEE MILCOM*, pp. 487–492, IEEE, 2005.

[44] G. Jakllari, W. Luo, and S. V. Krishnamurthy, "An integrated neighbor discovery and mac protocol for ad hoc networks using directional antennas," *Wireless Communications, IEEE Transactions on*, vol. 6, no. 3, pp. 1114–1024, 2007.

[45] M. Khan, S. Bhunia, M. Yuksel, and S. Sengupta, "Los discovery in 3d for highly directional transceivers," in *Military Communications Conference, MILCOM 2016-2016 IEEE*, pp. 325–330, IEEE, 2016.

[46] P. Deng, M. Kavehrad, and Y. Lou, "Mems-based beam-steerable fso communications for reconfigurable wireless data center," in *Broadband Access Communication Technologies XI*, vol. 10128, p. 1012805, International Society for Optics and Photonics, 2017.

[47] P. Deng, T. Kane, and O. Alharbi, "Reconfigurable free space optical data center network using gimbal-less mems retroreflective acquisition and tracking," in *Free-Space Laser Com-*

munication and Atmospheric Propagation XXX, vol. 10524, p. 1052403, International Society for Optics and Photonics, 2018.

[48] B. Winker, M. Mahajan, and M. Hunwardsen, "Liquid crystal beam directors for airborne free-space optical communications," in *2004 IEEE Aerospace Conference Proceedings (IEEE Cat. No. 04TH8720)*, vol. 3, IEEE, 2004.

[49] R. Fatemi, A. Khachaturian, and A. Hajimiri, "A low power pwm optical phased array transmitter with 16° field-of-view and 0.8° beamwidth," in *2018 IEEE Radio Frequency Integrated Circuits Symposium (RFIC)*, pp. 28–31, IEEE, 2018.

[50] T. Koonen, F. Gomez-Agis, F. Huijskens, K. A. Mekonnen, Z. Cao, and E. Tangdiongga, "High-capacity optical wireless communication using two-dimensional ir beam steering," *Journal of Lightwave Technology*, vol. 36, no. 19, pp. 4486–4493, 2018.

[51] T. Koonen, "Indoor optical wireless systems: technology, trends, and applications," *Journal of Lightwave Technology*, vol. 36, no. 8, pp. 1459–1467, 2017.

[52] P. De La Llana, A. S. Haq, and M. Yuksel, "Design of a multi-element fso transceiver array for mobile communication links," in *Free-Space Laser Communications XXXIII*, vol. 11678, p. 1167805, International Society for Optics and Photonics, 2021.

[53] J. Akella, M. Yuksel, and S. Kalyanaraman, "Multi-element array antennas for free-space optical communication," in *Second IFIP International Conference on Wireless and Optical Communications Networks, 2005. WOCN 2005.*, pp. 159–163, IEEE, 2005.

[54] M. Bilgi and M. Yuksel, "Multi-element free-space-optical spherical structures with intermittent connectivity patterns," in *IEEE INFOCOM Workshops 2008*, pp. 1–4, IEEE, 2008.

[55] A. Kaadan, H. H. Refai, and P. G. LoPresti, "Multielement FSO transceivers alignment for inter-UAV communications," *Journal of Lightwave Technology*, vol. 32, no. 24, pp. 4785–4795, 2014.

[56] Y. S. Eroğlu, I. Güvenç, N. Pala, and M. Yuksel, "AOA-based localization and tracking in multi-element VLC systems," in *2015 IEEE 16th annual wireless and microwave technology conference (WAMICON)*, pp. 1–5, IEEE, 2015.

[57] Y. S. Eroğlu, I. Güvenç, A. Şahin, Y. Yapıcı, N. Pala, and M. Yuksel, "Multi-element VLC networks: LED assignment, power control, and optimum combining," *IEEE Journal on Selected Areas in Communications*, vol. 36, no. 1, pp. 121–135, 2017.

[58] S. I. Mushfique, A. Alsharoa, and M. Yuksel, "Optimization of sinr and illumination uniformity in multi-led multi-datastream vlc networks," *IEEE Transactions on Cognitive Communications and Networking*, 2020.

[59] A. Desai and S. Milner, "Autonomous reconfiguration in free-space optical sensor networks," *IEEE Journal on Selected Areas in Communications*, vol. 23, no. 8, pp. 1556–1563, 2005.

[60] B. Edwards, "Overview of the laser communications relay demonstration project," in *SpaceOps 2012*, p. 1261897, 2012.

[61] B. Moision, B. Erkmen, E. Keyes, T. Belt, O. Bowen, D. Brinkley, P. Csonka, M. Eglington, A. Kazmierski, N.-h. Kim, *et al.*, "Demonstration of free-space optical communication for long-range data links between balloons on project loon," in *Free-Space Laser Communication and Atmospheric Propagation XXIX*, vol. 10096, p. 100960Z, International Society for Optics and Photonics, 2017.

[62] A. U. Chaudhry and H. Yanikomeroglu, "Laser intersatellite links in a starlink constellation: A classification and analysis," *IEEE Vehicular Technology Magazine*, vol. 16, no. 2, pp. 48–56, 2021.

[63] A. F. M. S. Haq and M. Yuksel, "Weather-limited in-band full-duplex transceiver model for free-space optical communication," *Optical Engineering*, vol. 59, no. 5, p. 056113, 2020.

[64] A. S. Haq and M. Yuksel, "Weather limited short-range in-band full-duplex free-space optical transceiver," in *Free-Space Laser Communications XXXI*, vol. 10910, p. 1091021, International Society for Optics and Photonics, 2019.

[65] V. Abhayawardhana, I. Wassell, D. Crosby, M. Sellars, and M. Brown, "Comparison of empirical propagation path loss models for fixed wireless access systems," in *Vehicular Technology Conference, 2005. VTC 2005-Spring. 2005 IEEE 61st*, vol. 1, pp. 73–77, IEEE, 2005.

[66] H. Manor and S. Arnon, "Performance of an optical wireless communication system as a function of wavelength," *Applied optics*, vol. 42, no. 21, pp. 4285–4294, 2003.

[67] D. C. O'Brien, M. Katz, P. Wang, K. Kalliojarvi, S. Arnon, M. Matsumoto, R. Green, and S. Jivkova, "Short-range optical wireless communications," in *Wireless world research forum*, pp. 1–22, 2005.

[68] H. Weichel, *Laser beam propagation in the atmosphere*, vol. 3. SPIE press, 1990.

[69] I. I. Kim, B. McArthur, and E. J. Korevaar, "Comparison of laser beam propagation at 785 nm and 1550 nm in fog and haze for optical wireless communications," in *Optical Wireless Communications III*, vol. 4214, pp. 26–38, International Society for Optics and Photonics, 2001.

[70] S. G. Lambert and W. L. Casey, *Laser communications in space*. Artech House, 1995.

[71] N. S. Kopeika, *A system engineering approach to imaging*. SPIE Optical Engineering Press Bellingham, 1998.

[72] A. Yariv, *Optical electronics*. Saunders College Publ., 1991.

[73] S. Leclercq, "Discussion about noise equivalent power and its use for photonnoise calculation," *Report On FOV Optics And Bolometer Projects For The 30m Telescope, International Research Institute For Radio Astronomy (IRAM)*, pp. 1–15, 2007.

[74] J. W. Giles and I. N. Bankman, "Underwater optical communications systems. part 2: Basic design considerations," in *MILCOM 2005-2005 IEEE Military Comm. Conf.*, pp. 1700–1705, IEEE, 2005.

[75] M. Duarte, C. Dick, and A. Sabharwal, "Experiment-driven characterization of full-duplex wireless systems," *IEEE Transactions on Wireless Communications*, vol. 11, no. 12, pp. 4296–4307, 2012.

[76] K. Akcapinar and O. Gurbuz, "Full-duplex bidirectional communication under self-interference," in *Telecommunications (ConTEL), 2015 13th International Conference on*, pp. 1–7, IEEE, 2015.

[77] A. S. Haq, M. R. Khan, and M. Yuksel, "A prototype of in-band full-duplex free-space optical transceiver," in *2018 IEEE International Symposium on Local and Metropolitan Area Networks (LANMAN)*, pp. 112–113, IEEE, 2018.

[78] P. S. Cross and H. Kogelnik, "Sidelobe suppression in corrugated-waveguide filters," *Optices Letter*, vol. 1, no. 1, pp. 43–45, 1977.

[79] C. Guclu, S. Campione, O. Boyraz, and F. Capolino, "Theory of a directive optical leaky wave antenna integrated into a resonator and enhancement of radiation control," *Journal of Lightwave Technology*, vol. 32, no. 9, pp. 1741–1749, 2014.

[80] S. Mori, "Side lobe suppression of a bessel beam for high aspect ratio laser processing," *Precision Engineering*, vol. 39, pp. 79–85, 2015.

[81] J. R. Leger, G. J. Swanson, and M. Holz, "Efficient side lobe suppression of laser diode arrays," *Applied physics letters*, vol. 50, no. 16, pp. 1044–1046, 1987.

[82] "Raspberry pi 3 model b." https://www.raspberrypi.org/products/raspberry-pi-3-model-b/.

[83] "IrDA2 click." http://www.mikroe.com/click/irda2/.

[84] "Python." https://www.python.org/.

[85] A. F. M. S. Haq, M. Khan, and M. Yuksel, "Asynchronous LOS discovery algorithm for aerial nodes using in-band full-duplex transceivers," in *Proceedings of the 15th International CoNEXT*, ACM, 2019.

[86] M. R. Khan, S. Bhunia, M. Yuksel, and L. Kane, "Line-of-sight discovery in 3d using highly directional transceivers," *IEEE Transactions on Mobile Computing*, 2018.

[87] M. Khan and M. Yuksel, "In-band LOS discovery between drones using highly directional transceivers," in *Proceedings of the 4th ACM Workshop on Micro Aerial Vehicle Networks, Systems, and Applications*, pp. 51–56, ACM, 2018.

[88] A. A. Farid and S. Hranilovic, "Outage capacity optimization for free-space optical links with pointing errors," *Journal of Lightwave technology*, vol. 25, no. 7, pp. 1702–1710, 2007.

[89] L. C. Andrews and R. L. Phillips, "Laser beam propagation through random media," SPIE, 2005.

[90] S. S. Polkoo and C. K. Renshaw, "Imaging-based beam steering for free-space optical communication," *Applied optics*, vol. 58, no. 13, pp. D12–D21, 2019.